

Finite temperature detection of quantum critical points via internal quantum teleportation

G. A. P. Ribeiro and Gustavo Rigolin*

Departamento de Física, Universidade Federal de São Carlos, 13565-905, São Carlos, SP, Brazil

(Dated: January 7, 2025)

We show that the teleportation protocol can be efficiently used to detect quantum critical points using finite temperature data even if all resources needed for its implementation lie within the system under investigation. Contrary to a previous proposal, there is no need to use an external qubit as the input state to be teleported to one of the qubits within the system. Here, we use a pair of nearest neighbor spins from an infinite spin-1/2 chain in equilibrium with a heat bath as the entangled resource of the quantum teleportation protocol and a third adjacent qubit within the chain itself as the input state to be teleported. For several spin chain models subjected to an external magnetic field, we show that the efficiency of the teleportation protocol is severely affected as we cross the quantum critical points associated with those spin chains. This abrupt change in efficiency gives us a clear indication of a quantum phase transition.

I. INTRODUCTION

The qualitative change in the macroscopic properties of a many-body system that occurs at the absolute zero temperature ($T = 0$) as we change its Hamiltonian is called a quantum phase transition (QPT). Theoretically it is described by the change of the many-body system's ground state as we slowly (adiabatically) modify its Hamiltonian (H) [1–4]. Since at $T = 0$ there are no thermal fluctuations, this change in the physical properties of the many-body system is caused by quantum fluctuations whose origin can be traced back to the Heisenberg uncertainty principle. A standard example of a QPT is the onset of a non-null magnetization when a spin chain enters its ferromagnetic phase coming from the paramagnetic one. In general, a QPT is given by a symmetry change in the ground state of the system and the appearance of an order parameter (the non-null magnetization in the above example).

Many important quantum information theory quantities were shown to be excellent quantum critical point (QCP) detectors at $T = 0$ [5–18]. However, it is known that some of them do not work properly when $T > 0$. For example, the entanglement of formation [19] between a pair of spins that belongs to a spin chain is zero before, at, and after the QCP if the chain is prepared above a certain threshold temperature [20, 21]. Therefore, both from a theoretical point of view and from practical aspects (we cannot cool a many-body system to $T = 0$ due to the third law of thermodynamics), it is important to develop robust tools to characterize QPTs at finite T . In this case thermal fluctuations are present and we must have tools to detect QCPs that properly work in this scenario.

One of the most successful and resilient tool to pinpoint a QCP at finite T is quantum discord (QD) [21], origi-

nally defined in Refs. [22, 23]. From a theoretical point of view, though, the computation of QD is not feasible for high spin systems. The evaluation of QD is an NP-complete problem [24], which means that the evaluation of QD becomes intractable as we increase the system's Hilbert space dimension. Even for spin-1 systems one already faces great challenges to compute it [25]. Moreover, from an experimental point of view, QD has no operational meaning. So far there is no general experimental procedure to directly measure QD. The determination of QD for a given system can only be achieved after we obtain either theoretically or experimentally its complete density matrix.

In Ref. [26] we went one step further and presented QCP detection tools that keep the most useful features of QD in detecting QCPs at finite T but do not have its theoretical and experimental handicaps outlined above. These tools are based on the quantum teleportation protocol [27–29] and are scalable to high dimensional systems, have a clear experimental meaning, and work at temperatures where other tools, such as the entanglement of formation, already fail to spotlight QCPs. See also Refs. [30–33] for other applications of the quantum teleportation protocol in spin chains, in particular the teleportation of a quantum state between distant spins of the chain.

In this work we show, under very general conditions, that we can simplify the tools to detect QCPs at finite T given in Ref. [26], while still keeping their efficiency, robustness, and scalability. In the present proposal, we do not need an external qubit from the system to implement the teleportation based QCP detector. We do not even need to repeat the procedure using several different external qubits covering the whole Bloch sphere in order to detect a QCP [26]. In the present proposal, the input state to be teleported is now fixed and belongs to the many-body system itself (see Fig. 1). Also, and similarly to the tool developed in Ref. [26], we do not need to know the order parameter associated with the QPT to implement it (see Refs. [21, 26] for more details).

Being more specific, we study the ability of the present

*Electronic address: rigolin@ufscar.br

tools, developed in Sec. II, to detect QCPs at finite or zero temperature for several spin-1/2 chains in the thermodynamic limit (infinite chains). We study the XXZ model subjected to a longitudinal external magnetic field in Sec. III and the Ising model and the XY model in a transverse magnetic field in Sec. IV. We end this work by giving in Sec. V an extensive analysis of the theoretical and experimental resources needed to apply these tools and in Sec. VI we provide our concluding remarks.

II. THE CRITICAL POINT DETECTOR

A. General settings

The key ingredient in our QCP detector is the standard teleportation protocol [27], expressed in the mathematical language of density matrices instead of pure states [26, 29, 34]. The entangled resource shared by Alice and Bob is given by qubits 2 and 3, respectively, and are described by the density matrix ρ_{23} . Alice's input qubit, the one to be teleported to Bob, is given by the density matrix ρ_1 . See Fig. 1 for a step by step description of the protocol.

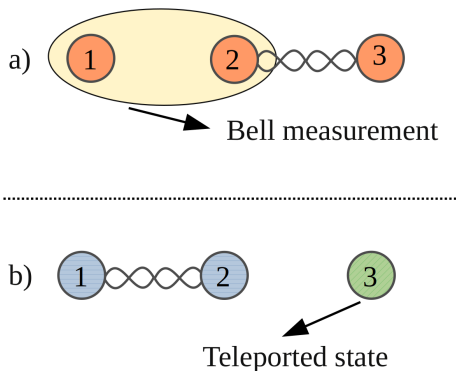


FIG. 1: (color online) One run of the teleportation protocol can be essentially divided into four steps, condensed in the two panels above. First, Alice and Bob share an entangled resource (qubits 2 and 3) and Alice choose a qubit to be teleported (qubit 1). Second, Alice implements a Bell measurement (BM) on qubits 1 and 2. A BM is a joint measurement on the qubit to be teleported to Bob and on one of the qubits of the entangled state shared with Bob. This step of the protocol is depicted in panel (a) above. Third, Alice informs Bob of her measurement result. There are four possibilities here and she needs to send two classical bits to Bob in order to tell him about which Bell state she measured. Fourth, Bob applies an appropriate unitary operation on his qubit depending on which Bell state Alice measured. After this step, the protocol ends and it is illustrated in panel (b). Bob's qubit at the end of a run of the protocol is more or less similar to Alice's original input state according to the quality of the shared entangled state between them (qubits 2 and 3).

Initially, the total state describing the three qubits par-

ticipating in the teleportation protocol is

$$\rho = \rho_1 \otimes \rho_{23} \quad (1)$$

and after one run of the protocol Bob's qubit is [26, 29]

$$\rho_{B_j} = \frac{U_j Tr_{12}[P_j \rho P_j] U_j^\dagger}{Q_j}. \quad (2)$$

In Eq. (2), Tr_{12} is the partial trace over Alice's qubits (spins 1 and 2), j is the Bell measurement (BM) outcome obtained by Alice ($j = \Psi^\pm, \Phi^\pm$), and P_j denotes the four projectors associated with the BMs,

$$P_{\Psi^\pm} = |\Psi^\pm\rangle\langle\Psi^\pm|, \quad (3)$$

$$P_{\Phi^\pm} = |\Phi^\pm\rangle\langle\Phi^\pm|, \quad (4)$$

where

$$|\Psi^\pm\rangle = (|01\rangle \pm |10\rangle)/\sqrt{2}, \quad (5)$$

$$|\Phi^\pm\rangle = (|00\rangle \pm |11\rangle)/\sqrt{2}. \quad (6)$$

The states given by Eqs. (5)-(6) are the four Bell states.

The other two quantities appearing in Eq. (2) are Alice's probability to obtain a certain Bell state j [26, 29],

$$Q_j = Tr[P_j \rho], \quad (7)$$

and the unitary correction U_j that Bob must apply on his qubit after being informed by Alice of her measurement outcome.

The unitary correction U_j that Bob must implement on his qubit after a run of the protocol depends not only on Alice's measurement result but also on the entangled state ρ_{23} shared with Alice. The sets S_k below give the unitary operations that Bob must apply on his qubit if the shared state between Alice and Bob is the Bell state $|k\rangle$ [26, 29],

$$S_{\Phi^+} = \{U_{\Phi^+}, U_{\Phi^-}, U_{\Psi^+}, U_{\Psi^-}\} = \{\mathbb{1}, \sigma^z, \sigma^x, \sigma^z \sigma^x\}, \quad (8)$$

$$S_{\Phi^-} = \{U_{\Phi^+}, U_{\Phi^-}, U_{\Psi^+}, U_{\Psi^-}\} = \{\sigma^z, \mathbb{1}, \sigma^z \sigma^x, \sigma^x\}, \quad (9)$$

$$S_{\Psi^+} = \{U_{\Phi^+}, U_{\Phi^-}, U_{\Psi^+}, U_{\Psi^-}\} = \{\sigma^z, \sigma^z \sigma^x, \mathbb{1}, \sigma^z\}, \quad (10)$$

$$S_{\Psi^-} = \{U_{\Phi^+}, U_{\Phi^-}, U_{\Psi^+}, U_{\Psi^-}\} = \{\sigma^z \sigma^x, \sigma^x, \sigma^z, \mathbb{1}\}. \quad (11)$$

Note that $\mathbb{1}$ is the identity matrix and σ^α , with $\alpha = x, y, z$, is the standard Pauli matrix [35].

The state ρ_{23} shared between Alice and Bob depends on the system's quantum phase. In one quantum phase ρ_{23} is more similar to one of the four Bell states while in a different quantum phase it is best approximated by another one. Hence, in order to better characterize the QCPs of a spin chain we will use the four sets S_k of unitary operations and also determine the set that gives the most efficient teleportation protocol within a quantum phase.

The efficiency of the teleportation protocol is given by how close the output state ρ_{B_j} is to the input state ρ_1 at the end of a run of the protocol. Therefore, in order to quantitatively assess that efficiency, we need to choose

quantitative measures of the similarity between the teleported state at the end of the protocol and the initial input state with Alice.

In this work we will be dealing with two measures that quantify the similarity between those two states. The first one is the fidelity [36], which is given by [35]

$$F_j(S_k) = F(\rho_1, \rho_{B_j}) = \left[\text{Tr} \sqrt{\sqrt{\rho_1} \rho_{B_j} \sqrt{\rho_1}} \right]^2. \quad (12)$$

In the left hand side of Eq. (12) we made it explicit that the fidelity also depends on the set S_k of unitary operations that Bob must apply on his qubit. If the teleported state is exactly equal to Alice's input state, we obtain $F_j = 1$, and $F_j = 0$ if those states are orthogonal. Note that in Ref. [35] the fidelity is defined as $\text{Tr} \sqrt{\sqrt{\rho_1} \rho_{B_j} \sqrt{\rho_1}}$. Here we take the square of the previous expression to conform with the definition used in our previous works when the input state was a pure state [26] and with the original work of Uhlmann [36].

After several implementations (runs) of the protocol, the mean fidelity (or efficiency of the protocol) is [26, 29, 34, 37]

$$\overline{F}(S_k) = \sum_{j=\Psi^\mp, \Phi^\mp} Q_j F_j(S_k). \quad (13)$$

Similarly to Ref. [26], Eq. (13) is the basic building block from which one teleportation based QCP detector is built. In particular, it is defined as the maximum mean fidelity [26]

$$\overline{\mathcal{F}} = \max_{\{S_k\}} \overline{F}(S_k). \quad (14)$$

As we will show in the next sections, the functional behavior of $\overline{\mathcal{F}}$ and of its first and second order derivatives in terms of the tuning parameter that drives the change in the system's Hamiltonian is a very useful QCP detector at zero and finite temperatures.

The second measure we will be using in this work to quantify the similarity between two mixed states is the trace distance [35, 38, 39],

$$D_j(S_k) = D(\rho_1, \rho_{B_j}) = \frac{1}{2} \text{Tr} \left| \rho_1 - \rho_{B_j} \right|, \quad (15)$$

where for an operator A we have $|A| = \sqrt{A^\dagger A}$. A direct computation for spin-1/2 density matrices gives

$$D_j(S_k) = \frac{1}{2} \sqrt{(\Delta r_x)^2 + (\Delta r_y)^2 + (\Delta r_z)^2}, \quad (16)$$

where $\Delta r_\alpha(t) = \text{Tr}(\rho_1 \sigma^\alpha) - \text{Tr}(\rho_{B_j} \sigma^\alpha)$, with σ^α being a Pauli matrix. Geometrically, the trace distance is half the Euclidean distance between the points on the Bloch sphere associated with the density matrices ρ_1 and ρ_{B_j} [35]. Therefore, when the two states are equal we have $D_j = 0$ and the farther apart the two states are in the Bloch sphere the greater D_j is. For orthogonal pure

states we have $D_j = 1$, the maximum possible value for the trace distance.

After several runs of the teleportation protocol, the mean trace distance is given by

$$\overline{D}(S_k) = \sum_{j=\Psi^\mp, \Phi^\mp} Q_j D_j(S_k) \quad (17)$$

and the second QCP point detector is built by minimizing $\overline{D}(S_k)$ over all sets S_k ,

$$\overline{D} = \min_{\{S_k\}} \overline{D}(S_k). \quad (18)$$

Similarly to $\overline{\mathcal{F}}$, the behavior of \overline{D} and of its first and second order derivatives with respect to the Hamiltonian's driving parameter turns out to be a very robust QCP detector at zero and finite temperatures.

Remark 1: Note that a high value for the fidelity between two states implies a low value for the trace distance and vice-versa. The fidelity measures the similarity between two states; the more similar the states the greater the fidelity. The trace distance, as its name suggests, measures the distance between those two states; the closer the states the lower the value of the trace distance. This is why for the fidelity we implement a maximization operation while for the trace distance we implement a minimization one.

Remark 2: The reason we use in this work the trace distance in addition to the fidelity to assess the efficiency of the teleportation protocol is related to two facts. First, the expressions for the fidelity between two mixed states are too cumbersome and complicated, while the expressions for the trace distance are relatively simpler. Second, the fidelity is less efficient than the trace distance to detect one of the QCPs of the XXZ model (see Sec. III). For the other models and the other QCP of the XXZ model, both quantities are for all practical purposes equivalent.

B. Specific settings

All the models we study here (Secs. III and IV) are one dimensional spin-1/2 chains in the thermodynamic limit ($L \rightarrow \infty$) satisfying periodic boundary conditions ($\sigma_{L+1}^\alpha = \sigma_1^\alpha$). Here the subscript implies that σ_j^α acts on the qubit located at the lattice site j . Also, all spin chains are assumed to be in equilibrium with a heat bath (thermal reservoir at temperature T) and, as such, the density matrix describing the whole chain is given by the canonical ensemble density matrix

$$\varrho = e^{-H/kT} / Z, \quad (19)$$

with $Z = \text{Tr}[e^{-H/kT}]$ being the partition function and k the Boltzmann's constant.

The density matrix describing three nearest neighbors from the spin chain is given by ρ_{123} , which is obtained by tracing out from ϱ all but spins 1, 2 and 3. Note that the initial state ρ_{123} can be obtained using any three nearest

neighbors from the spin chain. After putting the whole chain in contact with a heat reservoir at temperature T and waiting for the system to reach the thermodynamic equilibrium, any three consecutive spins of the chain can be used to implement the internal teleportation protocol as described below.

The density matrix ρ_{123} is in general not given by Eq. (1), where ρ_1 is given by tracing out from ϱ all but spin 1 and ρ_{23} is the state obtained by tracing out from ϱ all but spins 2 and 3. The state ρ_1 describes a single spin from the chain and ρ_{23} any nearest neighbor pair of spins from the chain. We have, therefore, to prepare an ensemble from ρ_{123} that is effectively given by Eq. (1). Before we explain how this can be done, we first give the explicit forms of ρ_{23} and ρ_1 in the standard basis.

For all the models investigated here we have [6, 21, 26]

$$\rho_{23} = \begin{pmatrix} a & 0 & 0 & e \\ 0 & b & c & 0 \\ 0 & c & b & 0 \\ e & 0 & 0 & d \end{pmatrix}, \quad (20)$$

where

$$a = \frac{1 + 2 \langle \sigma_2^z \rangle + \langle \sigma_2^z \sigma_3^z \rangle}{4}, \quad (21)$$

$$b = \frac{1 - \langle \sigma_2^z \sigma_3^z \rangle}{4}, \quad (22)$$

$$c = \frac{\langle \sigma_2^x \sigma_3^x \rangle + \langle \sigma_2^y \sigma_3^y \rangle}{4}, \quad (23)$$

$$d = \frac{1 - 2 \langle \sigma_2^z \rangle + \langle \sigma_2^z \sigma_3^z \rangle}{4}, \quad (24)$$

$$e = \frac{\langle \sigma_2^x \sigma_3^x \rangle - \langle \sigma_2^y \sigma_3^y \rangle}{4}. \quad (25)$$

For the XXZ and XX models $\langle \sigma_2^x \sigma_3^x \rangle = \langle \sigma_2^y \sigma_3^y \rangle$ while for the Ising and XY models $\langle \sigma_2^x \sigma_3^x \rangle \neq \langle \sigma_2^y \sigma_3^y \rangle$. We should also note that the translational invariance of the spin chain implies that $\langle \sigma_j^\alpha \rangle = \langle \sigma_k^\alpha \rangle$ and $\langle \sigma_j^\alpha \sigma_{j+1}^\beta \rangle = \langle \sigma_k^\alpha \sigma_{k+1}^\beta \rangle$, for any value of j, k .

The evaluation in the thermodynamic limit and for arbitrary values of T of the one-point and two-point correlation functions,

$$z = \langle \sigma_j^z \rangle = \text{Tr}[\sigma_j^z \varrho], \quad (26)$$

$$\alpha\alpha = \langle \sigma_j^\alpha \sigma_{j+1}^\alpha \rangle = \text{Tr}[\sigma_j^\alpha \sigma_{j+1}^\alpha \varrho], \quad (27)$$

where $\alpha = x, y, z$, can be found in Refs. [40–52]. In Ref. [21] these calculations are reviewed and written in the present notation. The behavior of $\langle \sigma_j^z \rangle$ and $\langle \sigma_j^\alpha \sigma_{j+1}^\alpha \rangle$ for several values of T as we change the tuning parameter for each one of the models given in Secs. III and IV are shown in Ref. [26].

The density matrix ρ_1 describing a single spin is calculated by tracing out from the thermal state ϱ [Eq. (19)] all but one spin. Or, equivalently, by tracing out one of the spins from ρ_{23} . Therefore, a simple calculation gives

$$\rho_1 = \begin{pmatrix} p_0 & 0 \\ 0 & p_1 \end{pmatrix} = p_0 |0\rangle\langle 0| + p_1 |1\rangle\langle 1|, \quad (28)$$

where

$$p_0 = \frac{1 + \langle \sigma^z \rangle}{2}, \quad (29)$$

$$p_1 = \frac{1 - \langle \sigma^z \rangle}{2}. \quad (30)$$

In Eqs. (29) and (30) we have dropped the subscript from the one-point correlation function for simplicity.

Using Eq. (28) and that

$$\rho_{23} = \text{Tr}_1[\rho_{123}] = {}_1\langle 0|\rho_{123}|0\rangle_1 + {}_1\langle 1|\rho_{123}|1\rangle_1,$$

the state (1) can be written as follows,

$$\begin{aligned} \rho = & p_0 |0\rangle_1 {}_1\langle 0| \otimes {}_1\langle 0|\rho_{123}|0\rangle_1 \\ & + p_0 |0\rangle_1 {}_1\langle 1| \otimes {}_1\langle 1|\rho_{123}|1\rangle_1 \\ & + p_1 |1\rangle_1 {}_1\langle 1| \otimes {}_1\langle 0|\rho_{123}|0\rangle_1 \\ & + p_1 |1\rangle_1 {}_1\langle 1| \otimes {}_1\langle 1|\rho_{123}|1\rangle_1. \end{aligned} \quad (31)$$

Writing ρ as given by Eq. (31) readily suggests the steps Alice needs to do to effectively obtain state (1). She projects qubit 1 in the computational basis. She obtains either $|0\rangle_1$ or $|1\rangle_1$ with probabilities p_0 and p_1 , respectively. According to the measurement postulate of quantum mechanics [35], the state ρ_{123} changes in each case to

$$\rho_{123} \rightarrow \frac{P_{|0\rangle} \rho_{123} P_{|0\rangle}}{p_0} = |0\rangle_1 {}_1\langle 0| \otimes \frac{{}_1\langle 0|\rho_{123}|0\rangle_1}{p_0}, \quad (32)$$

$$\rho_{123} \rightarrow \frac{P_{|1\rangle} \rho_{123} P_{|1\rangle}}{p_1} = |1\rangle_1 {}_1\langle 1| \otimes \frac{{}_1\langle 1|\rho_{123}|1\rangle_1}{p_1}, \quad (33)$$

where $P_{|j\rangle} = |j\rangle_1 {}_1\langle j|$, with $j = 0, 1$, is the projector onto the state $|j\rangle_1$.

Also, if after measuring her qubit Alice applies the spin flip unitary operation, namely, $\sigma_1^x |0(1)\rangle = |1(0)\rangle$, we have for each possible measurement result,

$$\rho_{123} \rightarrow \frac{\sigma_1^x P_{|0\rangle} \rho_{123} P_{|0\rangle} \sigma_1^x}{p_0} = |1\rangle_1 {}_1\langle 1| \otimes \frac{{}_1\langle 0|\rho_{123}|0\rangle_1}{p_0}, \quad (34)$$

$$\rho_{123} \rightarrow \frac{\sigma_1^x P_{|1\rangle} \rho_{123} P_{|1\rangle} \sigma_1^x}{p_1} = |0\rangle_1 {}_1\langle 0| \otimes \frac{{}_1\langle 1|\rho_{123}|1\rangle_1}{p_1}. \quad (35)$$

From four subensembles, each one with an equal number N of systems described by Eqs. (32), (33), (34), or (35), Alice builds the following ensemble. She picks $(p_0)^2 N$ states given by (32), $(p_1)^2 N$ states given by (33), $p_0 p_1 N$ states given by (34), and $p_0 p_1 N$ states given by (35). Combining these four subensembles leads to N states described by Eq. (31), or equivalently, Eq. (1).¹

¹ It is worth noticing that if Alice picks qubit 1 sufficiently away from qubits 2 and 3, the state ρ_{123} is already given by Eq. (1). Also, if we prepare two identical spin chains and pick qubit 1 from one chain and a pair of nearest neighbors from the other chain, we also have Eq. (1) describing those three qubits.

Note that due to the linearity of all the steps related to the implementation of the teleportation protocol, from the experimental point of view Alice's job to effectively obtain Eq. (1) is very simple. She just needs to measure the qubit 1 in the computational basis and then either do nothing or implement the bit flip operation before initiating the standard teleportation protocol as described in Sec. II A. Being more specific, if she measures $|0\rangle$ she does nothing to her qubit (p_0)² of the times or she flips it $p_0 p_1$ of the times before starting the teleportation protocol. If she measures $|1\rangle$, she does nothing (p_1)² of the times or she flips it $p_0 p_1$ of the times before implementing the teleportation protocol. Also, she must work with an equal number of cases where she measured $|0\rangle$ or $|1\rangle$ to mimic the state given by Eq. (31) following the prescription given above. This is easily accomplished discarding the exceeding cases.

The bottom line is that by proceeding as described above and due to the linearity of all the steps involved in the execution of the teleportation protocol, the effective initial state will be given by Eq. (1) and Bob's qubit at the end of several runs of the teleportation protocol will effectively be described by Eq. (2) whenever Alice measures the Bell state j . Figure 2 illustrates all the steps of a single run of the protocol.

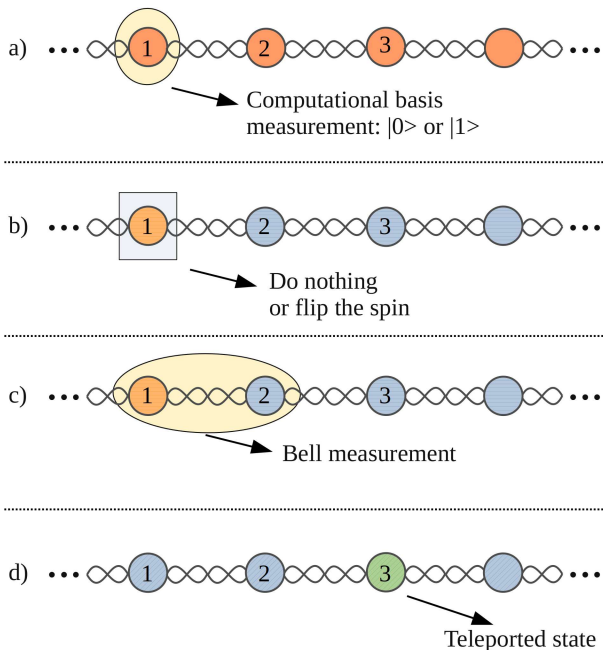


FIG. 2: (color online) One run of the internal teleportation protocol can be described as follows. First, Alice projects the qubit to be teleported (qubit 1) onto the computational basis [panel (a)]. Second, she either does nothing with her qubit or applies onto it the spin flip operation (σ_1^x) according to the prescription given in the text [panel (b)]. Third, Alice and Bob execute the standard teleportation protocol following the steps given in Fig. 1 [panels (c) and (d)].

Alternatively one could use the state ρ_{123} to theoretically simulate the execution of the internal teleportation protocol. The state ρ_{123} is a 8×8 matrix depending not only on one- and two-point correlation functions but also on the genuine three-point ones ($\langle \sigma_j^\alpha \sigma_{j+1}^\beta \sigma_{j+1}^\gamma \rangle$). Nevertheless, due to the factorization property of the correlation functions of the XXZ spin chain [44], the three-point correlations for this model can be expressed very non-trivially in terms of the one- and two-point correlations. However, the computation of the three-point correlation functions for finite temperature and for the other models here investigated is a quite involved task [44–46]. Thus, in order to test the usefulness of the internal teleportation QCP detector, we worked with an initial state that depends at most on two-point correlation functions of two consecutive spin. It would be very interesting to extend the present analysis to the case where the state ρ_{123} is used as the initial state. We believe that the internal teleportation QCP detector will also work in this case. Perhaps giving results even better than the ones reported here. We should also note that from the experimental point of view working with ρ_{123} is even simpler. In this case Alice will not need to project qubit 1 onto the computational basis or flip her spin before implementing the standard teleportation protocol.

We now return to the computation of the relevant quantities needed to assess the efficiency of the teleportation protocol. Inserting Eqs. (1), (3), (4), (20), and (28) into Eq. (7) gives

$$Q_{\Psi^\pm} = (1 - z^2)/4, \quad (36)$$

$$Q_{\Phi^\pm} = (1 + z^2)/4, \quad (37)$$

where z is given by Eq. (26).

Using now Eqs. (12), (36) and (37), the mean fidelity given by Eq. (13) becomes,

$$\overline{F}(S_{\Psi\pm}) = \frac{1}{8} \left(\sqrt{(1+z)f(zz, -z)} + \sqrt{(1-z)f(zz, z)} \right)^2 + \frac{1}{8} \left(\sqrt{(1-z)g(zz, z)} + \sqrt{(1+z)g(zz, -z)} \right)^2, \quad (38)$$

$$\overline{F}(S_{\Phi\pm}) = \frac{1}{8} \left(\sqrt{(1-z)f(zz, -z)} + \sqrt{(1+z)f(zz, z)} \right)^2 + \frac{1}{8} \left(\sqrt{(1+z)g(zz, z)} + \sqrt{(1-z)g(zz, -z)} \right)^2, \quad (39)$$

where

$$f(zz, z) = 1 + z + z^2 + z \cdot zz, \quad (40)$$

$$g(zz, z) = 1 - z - z^2 + z \cdot zz. \quad (41)$$

Note that the dot between z and zz in Eqs. (40) and (41) means the standard multiplication between the one-point correlation function z and the two-point correlation function zz , Eqs. (26) and (27) respectively.

As anticipated in the second remark at the end of Sec. II A, the expressions for the fidelities are not simple and the maximum mean fidelity becomes

$$\overline{F} = \max [\overline{F}(S_{\Psi\pm}), \overline{F}(S_{\Phi\pm})], \quad (42)$$

with $\overline{F}(S_{\Psi\pm})$ and $\overline{F}(S_{\Phi\pm})$ given by Eqs. (38) and (39).

Equation (42) is the first teleportation based QCP detector we will be using in this work. The second one is based on the trace distance.

If we repeat the above calculation using Eqs. (16), (36) and (37), the mean trace distance given by Eq. (17) becomes,

$$\overline{D}(S_{\Psi\pm}) = \frac{1}{4} [(2 + z^2 + zz)|z| + |z^3 - z \cdot zz|], \quad (43)$$

$$\overline{D}(S_{\Phi\pm}) = \frac{1}{4} [(2 - z^2 - zz)|z| + |z^3 - z \cdot zz|], \quad (44)$$

and the minimum mean trace distance is according to Eq. (18) given by

$$\begin{aligned} \overline{D} &= \min [\overline{D}(S_{\Psi\pm}), \overline{D}(S_{\Phi\pm})] \\ &= \frac{1}{4} [(2 - |z^2 + zz|)|z| + |z^3 - z \cdot zz|]. \end{aligned} \quad (45)$$

Equation (45) is our second teleportation based QCP detector. In Secs. III and IV we investigate the effectiveness of both QCP detectors, Eqs. (42) and (45), in spotlighting the correct location of the QCP for several models at zero and non-zero temperatures.

Remark 3: Equations (42) and (45) do not depend on the two-point correlation functions $xx = \langle \sigma_j^x \sigma_{j+1}^x \rangle$ and $yy = \langle \sigma_j^y \sigma_{j+1}^y \rangle$, as can be seen by looking at Eqs. (38), (39), (43), and (44). The underlying reason for this is the specific form of ρ_1 [Eq. (28)]. Whenever the input state to be teleported is diagonal in the standard basis $\{|0\rangle, |1\rangle\}$, the expressions for the fidelity and for the trace distance will not depend on xx and yy if ρ_{23} is given by Eq. (20). For input states having non-diagonal terms, though, a direct calculation shows that both the fidelity and the trace distance will also depend on xx and yy .

Remark 4: Contrary to the scenario in which the qubit to be teleported is external to the spin chain [26], the expressions for the fidelity and for the trace distance now depend on the one-point correlation function $z = \langle \sigma_j^z \rangle$. This happens because in the present case (internal teleportation), the input state to be teleported is a function of z , as can be seen by looking at Eq. (28). And this implies that the teleported states with Bob are, according to Eq. (2),

$$\rho_{B_{\Psi\pm}}(S_{\Psi\pm}) = \frac{1}{2(1-z^2)} \begin{pmatrix} g(zz, -z) & 0 \\ 0 & g(zz, z) \end{pmatrix}, \quad (46)$$

$$\rho_{B_{\Phi\pm}}(S_{\Psi\pm}) = \frac{1}{2(1+z^2)} \begin{pmatrix} f(zz, -z) & 0 \\ 0 & f(zz, z) \end{pmatrix}, \quad (47)$$

$$\rho_{B_{\Psi\pm}}(S_{\Phi\pm}) = \frac{1}{2(1-z^2)} \begin{pmatrix} g(zz, z) & 0 \\ 0 & g(zz, -z) \end{pmatrix}, \quad (48)$$

$$\rho_{B_{\Phi\pm}}(S_{\Phi\pm}) = \frac{1}{2(1+z^2)} \begin{pmatrix} f(zz, z) & 0 \\ 0 & f(zz, -z) \end{pmatrix}, \quad (49)$$

where $f(zz, z)$ and $g(zz, z)$ are given by Eqs. (40) and (41), respectively. In Eqs. (46)-(49) we have explicitly written the dependence of Bob's final state on the set S_k containing the unitary corrections that he can implement on his qubit. In other words, $\rho_{B_j}(S_k)$ denotes the final state with Bob if Alice measures the Bell state j and Bob corrects his qubit using the corresponding unitary correction listed in S_k [cf. Eqs. (8)-(11)].

Remark 5: If we set $z = 0$, Eqs. (38), (39), (43), and (44) become $\overline{F}(S_{\Psi\pm}) = \overline{F}(S_{\Phi\pm}) = 1$ and $\overline{D}(S_{\Psi\pm}) = \overline{D}(S_{\Phi\pm}) = 0$. This means that the present method to detect QCPs does not work for the classes of spin chains studied here that do not have a net magnetization. For instance, it does not work for the XXZ model when the external magnetic field is zero since in this case we always have $z = 0$ as we drive the system across its QCPs [21, 26]. In other words, whenever $z = 0$ the output state with Bob at the end of the teleportation protocol will always be exactly equal to the input state of Alice regardless of the quantum phase of the system. We will always obtain the same constant values for the maximum mean fidelity ($\overline{F} = 1$) and for the minimum mean trace distance ($\overline{D} = 0$) in all quantum phases.

III. THE XXZ MODEL IN AN EXTERNAL FIELD

The XXZ spin chain in an external longitudinal magnetic field is described by the following Hamiltonian,

where we set $\hbar = 1$,

$$H = \sum_{j=1}^L \left(\sigma_j^x \sigma_{j+1}^x + \sigma_j^y \sigma_{j+1}^y + \Delta \sigma_j^z \sigma_{j+1}^z - \frac{h}{2} \sigma_j^z \right). \quad (50)$$

In Eq. (50) Δ is the tuning parameter and h is the external field.

The XXZ model has two QCPs at zero temperature [40–43, 45–47]. For a given field h , as we vary Δ we see at $\Delta = \Delta_1$ the first QPT, with the system's ground state changing from a ferromagnetic ($\Delta < \Delta_1$) to a critical antiferromagnetic phase ($\Delta_1 < \Delta < \Delta_2$). If we continue to increase Δ , we have at $\Delta = \Delta_2$ another QPT, where the spin chain becomes an Ising-like antiferromagnet.

The value of Δ_1 as a function of h is given by the solution of

$$h = 4J(1 + \Delta_1). \quad (51)$$

On the other hand, Δ_2 is obtained by solving the following equation,

$$h = 4 \sinh(\eta) \sum_{j=-\infty}^{\infty} \frac{(-1)^j}{\cosh(j\eta)}, \quad (52)$$

with $\eta = \cosh^{-1}(\Delta_2)$. For $h = 12$, the value of h adopted in this work, the two critical points are

$$\Delta_1 = 2.000, \quad (53)$$

$$\Delta_2 = 4.875, \quad (54)$$

with the latter QCP correct within a numerical error of ± 0.001 .

Let us start studying the efficacy of the maximum mean fidelity in detecting the two QCPs for the XXZ model in an external field. In Fig. 3 we show $\overline{\mathcal{F}}$ as a function of Δ for $h = 12$ and several values of T .

Looking at Fig. 3, we realize that $\overline{\mathcal{F}}$ clearly detects the first QCP, with an efficacy compatible to the one we have when employing the external teleportation approach of Ref. [26]. The detection of the second QCP, though, is not good enough. As we see in the inset of Fig. 3, we need to know the fidelity within an accuracy of 0.001 to observe a discontinuity in its derivative. And as we increase T , we rapidly lose any means of tracking the correct location of the second QCP.

This problem is solved by working with the trace distance. In Fig. 4 we show $\overline{\mathcal{D}}$ as a function of Δ for $h = 12$ and the same values of kT given in Fig. 3.

Looking at Fig. 4 we note that the two QCPs (Δ_1 and Δ_2) are clearly detected by discontinuities in the derivatives of $\overline{\mathcal{D}}$ with respect to Δ as we go through the critical points. Also, in contrast to the behavior of $\overline{\mathcal{F}}$ in the external teleportation approach [26], we do not see two extra discontinuities in the derivatives of $\overline{\mathcal{F}}$ and of $\overline{\mathcal{D}}$ [cf. Figs. 3 and 4 with the corresponding ones given in Ref. [26]]. In the present case, we only have one small kink between the two QCPs.

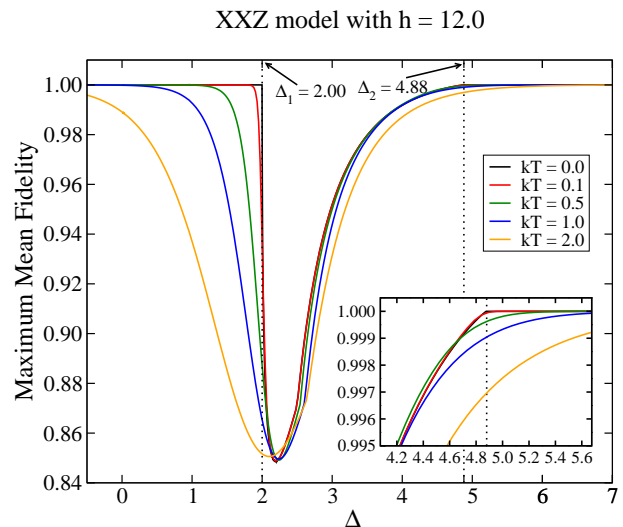


FIG. 3: (color online) $\overline{\mathcal{F}}$, Eq. (42), as a function of Δ for $h = 12.0$. At $T = 0$ both QCPs are detected by a discontinuity in the derivative of $\overline{\mathcal{F}}$ with respect to Δ . See the inset for a better appreciation of this fact at the second QCP. For $T > 0$, these discontinuities in the derivatives are smoothed out and manifest themselves in high values for the magnitudes of the derivatives around the critical points. The dotted lines mark the QCPs and for the solid curves the temperature increases from top to bottom when $\Delta < \Delta_1$. Here and in all other graphs all quantities are dimensionless.

This extra kink is related to the exchange of the functions maximizing $\overline{\mathcal{F}}$ or minimizing $\overline{\mathcal{D}}$ as we reach the location of that extra kink. In Fig. 5 we illustrate this point showing at $T = 0$ the two expressions appearing in the definition of $\overline{\mathcal{D}}$, Eqs. (43) and (44), as functions of Δ . Before the extra kink the expression minimizing $\overline{\mathcal{D}}$ is given by $\overline{\mathcal{D}}(S_{\Phi\pm})$ and after it we have $\overline{\mathcal{D}}(S_{\Psi\pm})$. The point where $\overline{\mathcal{D}}(S_{\Phi\pm})$ and $\overline{\mathcal{D}}(S_{\Psi\pm})$ intersect each other is exactly the point where we see the extra kink in the curve of $\overline{\mathcal{D}}$. Note also that the location of this extra kink changes as we increase the temperature and that the same analysis applies to the fidelity and to higher temperatures as well.

To estimate the values of the two QCPs using finite T data, we employ the same techniques of Refs. [21, 26]. For finite T , the $T = 0$ discontinuities in the derivatives of $\overline{\mathcal{D}}$ with respect to Δ at the QCPs manifest themselves in high values for the magnitudes of these derivatives around the QCPs. The location of these extremum values around the QCPs for several values of T are the key finite T data we need to obtain the QCPs. We can predict the values of the two QCPs by extrapolating to $T = 0$ how the locations of those extremum values change as we decrease the temperature.

Specifically, for six different temperatures, namely, $kT = 0, 0.1, 0.2, 0.3, 0.4$, and 0.5 , we calculated around the two critical points the values of the one- and two-point correlation functions and of $\overline{\mathcal{D}}$ as a function of Δ . We changed Δ in increments of 0.01. Afterwards, we numerically evaluated the first order derivatives of those

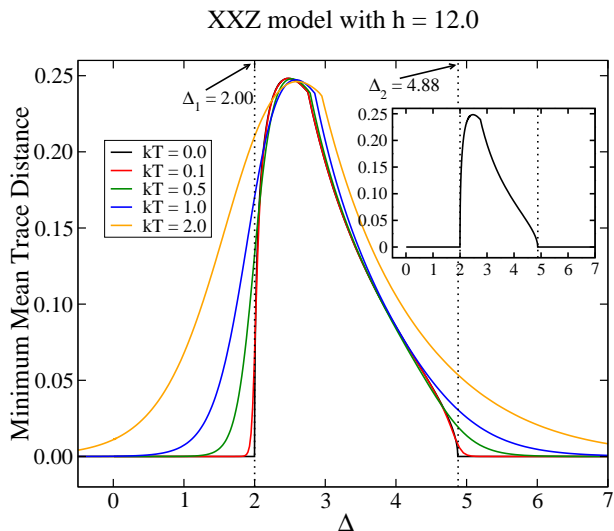


FIG. 4: (color online) \overline{D} , Eq. (45), as a function of Δ for $h = 12.0$. Note that now at $T = 0$ (see inset) both QCPs are clearly detected by a discontinuity in the derivative of \overline{D} with respect to Δ . For $T > 0$, there are no longer discontinuities in the derivatives. In this case we have high values for the derivatives about the location of the discontinuities that occurred at $T = 0$. For $kT \lesssim 0.5$, the extrema of the derivatives lie close together and by extrapolating to $kT \rightarrow 0$ we can correctly determine the QCPs. The dotted lines mark the exact locations of the QCPs and for the solid curves the temperature increases from bottom to top when $\Delta < \Delta_1$ and $\Delta > \Delta_2$.

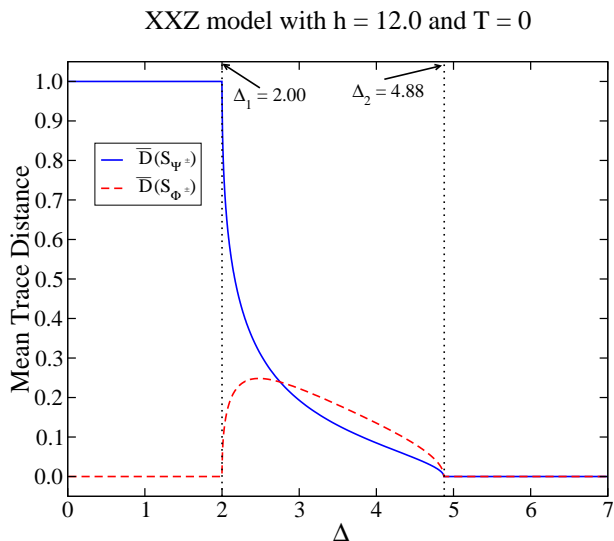


FIG. 5: (color online) $\overline{D}(S_k)$, Eqs. (43) and (44), as a function of Δ when $T = 0$ and $h = 12.0$.

quantities about Δ_1 and their second order derivatives about Δ_2 . The highest values for the magnitudes of those derivatives can be seen in Fig. 6. Moreover, taking into account that Δ was changed in increments of 0.01, the location of the maxima of the magnitudes of the first order derivatives are obtained with an error of ± 0.01 . On

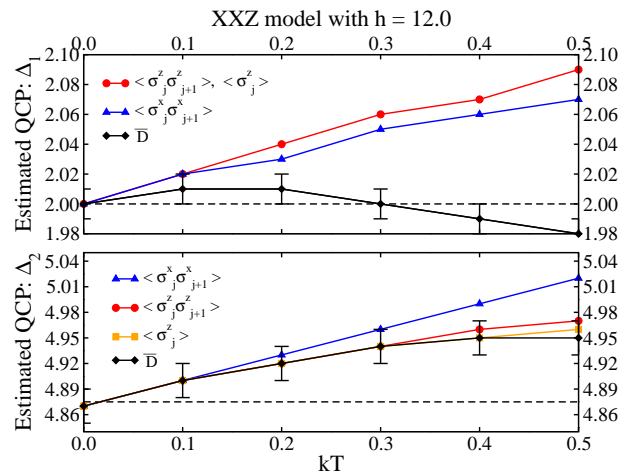


FIG. 6: (color online) Estimated QCPs after determining the spots of the extrema of the first order (upper panel) and of the second order (lower panel) derivatives with respect to Δ for \overline{D} , $\langle \sigma_j^x \sigma_{j+1}^x \rangle$, $\langle \sigma_j^z \sigma_{j+1}^z \rangle$, and $\langle \sigma_j^z \rangle$ at several different values of T . The dashed lines mark the exact values of the QCPs. The error bars in the curves showing the locations of the extrema of the derivatives of \overline{D} represent the numerical uncertainty in determining their exact location. For the other quantities in the two panels, similar error bars (not shown) exist about the dots showing the locations of the extrema of their derivatives. See text for details.

the other hand, the second order derivatives are calculated from the first order ones, which already possess an error of ± 0.01 . Therefore, we estimate that the error of the correct spot for the extremum values of the second order derivatives are no less than ± 0.02 . To not clutter the visualization of the other curves, in Fig. 6 we draw error bars depicting these uncertainties only for \overline{D} .

Looking at Fig. 6, we note that for all temperatures the extremum of the first order derivative of \overline{D} gives the best approximation for the exact value of the first QCP (upper panel of Fig. 6). The second QCP is also better approximated by the the extremum of the second order derivative of \overline{D} (lower panel of Fig. 6). However, as we decrease kT the other quantities shown in Fig. 6 catch up. Around $kT = 0.1$ they are all equally efficient in estimating the location of the second QCP. Also, remembering that for the external teleportation strategy the behavior of the derivatives of \overline{F} is equal to the behavior of the derivatives of $\langle \sigma_j^z \sigma_{j+1}^z \rangle$ [26], we have that the internal teleportation strategy gives better estimates for the location of the two QCPs when compared with the external teleportation approach.

Excluding the $kT = 0$ point, we can implement linear and quadratic regressions to find the best curves fitting the remaining data ($kT = 0.1, 0.2, 0.3, 0.4, 0.5$) [26]. For all quantities given in the lower panel of Fig. 6, a linear regression is enough to predict the correct location of the QCP Δ_2 as we take the $T = 0$ limit. The predicted location of Δ_2 is given within an accuracy of ± 0.02 , the estimated numerical error for the locations of the extrema of

the second order derivatives of all the quantities given in Fig. 6. The same conclusion applies for all but one of the curves given in the upper panel of Fig. 6, where again the fitted straight lines give the correct location of the QCP Δ_1 within an accuracy of ± 0.01 , the numerical error for the locations of the extrema of the first order derivatives of all the quantities given in Fig. 6. To achieve this same level of accuracy for $\overline{\mathcal{D}}$, though, we need a quadratic regression.

Remark 6: Although the results reported in this section were obtained assuming that the external magnetic field was $h = 12$, similar results are obtained for other values of the field.

Remark 7: Instead of using $\overline{\mathcal{D}}$ [Eq. (45)] and its derivatives to estimate the QCPs using finite T data, we could have worked directly with either $\overline{\mathcal{D}}(S_{\Phi\pm})$ or $\overline{\mathcal{D}}(S_{\Psi\pm})$ [Eq. (43) or (44)] and their derivatives. All three quantities give similar results in predicting the location of the QCPs.

IV. THE XY AND THE ISING MODEL

A spin-1/2 chain in an external transverse magnetic field described by the XY model is given by the following Hamiltonian [48–50],

$$H = -\frac{\lambda}{4} \sum_{j=1}^L [(1 + \gamma)\sigma_j^x \sigma_{j+1}^x + (1 - \gamma)\sigma_j^y \sigma_{j+1}^y] - \frac{1}{2} \sum_{j=1}^L \sigma_j^z. \quad (55)$$

In Eq. (55) λ is associated with the inverse of the strength of the magnetic field and γ is the anisotropy parameter. We obtain the Ising transverse model from Eq. (55) by setting $\gamma = \pm 1$. And if $\gamma = 0$ we have the XX model in a transverse magnetic field.

The tuning parameter for the present model can be either λ or γ . Fixing γ , we have that for $\lambda < 1$ the system is in a ferromagnetic ordered phase and as we increase λ we reach the QCP $\lambda_c = 1.0$, where the Ising transition occurs. For $\lambda > 1$ the system now lies in a quantum paramagnetic phase [51]. There is another QPT for this model when $\lambda > 1$ if we change the anisotropy parameter γ instead of λ . This “anisotropy transition” occurs at $\gamma_c = 0$ [48–50, 52], where the critical point γ_c separates a ferromagnet ordered phase in the x -direction from a ferromagnet ordered phase in the y -direction.

A. The λ transition

In Figs. 7, 8, and 9 we plot the maximum mean fidelity $\overline{\mathcal{F}}$ as a function of λ for three values of γ and for several values of temperature. The chosen values for γ are such that we obtain the isotropic XX model ($\gamma = 0.0$), the anisotropic XY model ($\gamma = 0.5$), and the Ising model ($\gamma = 1.0$).

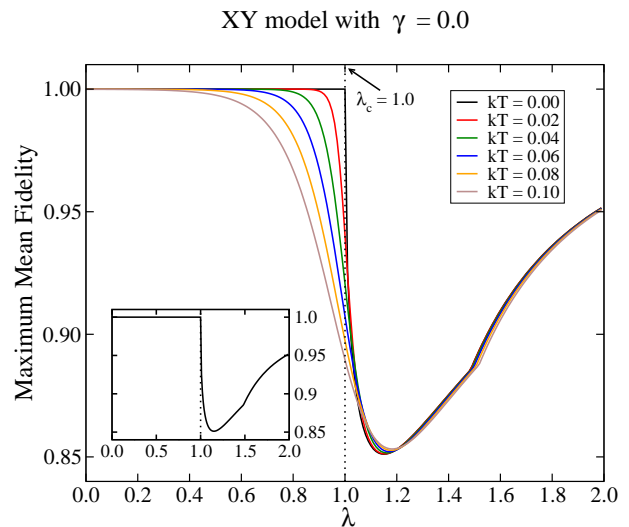


FIG. 7: (color online) $\overline{\mathcal{F}}$, Eq. (42), as a function of λ and for several values of kT when we fix $\gamma = 0.0$ (XX model in a transverse field) [see Eq. (55)]. The inset highlights the $T = 0$ curve. The dotted lines mark the QCP λ_c and for the solid curves the temperature increases from top to bottom when $\lambda < \lambda_c$.

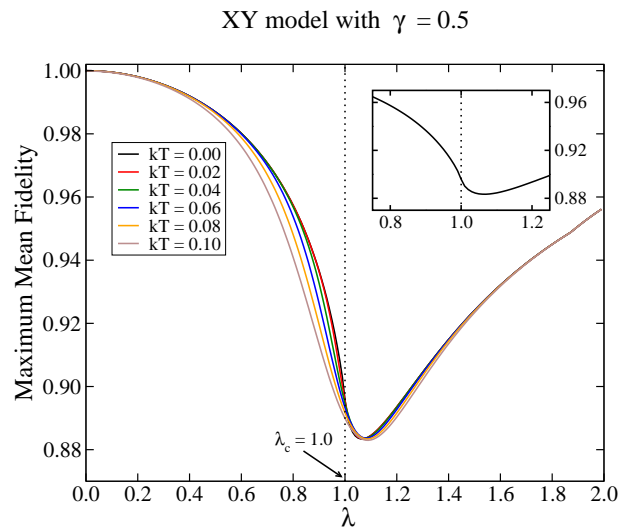


FIG. 8: (color online) Same as Fig. 7 but now $\gamma = 0.5$. The dotted lines mark the QCP λ_c and for the solid curves the temperature increases from top to bottom when $\lambda < \lambda_c$.

For the isotropic XX model ($\gamma = 0.0$), the QCP is clearly detect at $T = 0$ by a discontinuity in the derivative of $\overline{\mathcal{F}}$ at $\lambda_c = 1.0$ (see Fig. 7) as well as discontinuities in the derivatives of the one- and two-point correlation functions [26]. For $T > 0$, the discontinuity in the derivative manifests itself in a high value for the derivative’s magnitude about the QCP. The location of the extremum values of the derivatives move away from the QCP as we change T . Nevertheless, as we will see for $kT \lesssim 0.1$, these extrema lie close to the correct value of the QCP and we can properly infer the correct location of λ_c by

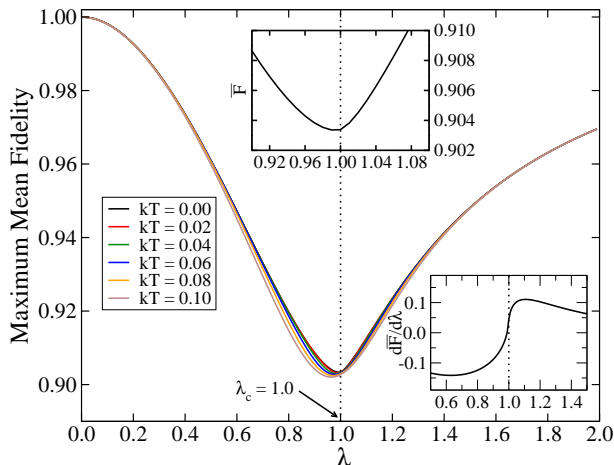
XY model with $\gamma = 1.0$ 

FIG. 9: (color online) Same as Fig. 7 but now $\gamma = 1.0$ (Ising model in a transverse field). The upper inset highlights the $T = 0$ curve of $\overline{\mathcal{F}}$ and the lower inset its derivative with respect to λ . The dotted lines mark the QCP λ_c and for the solid curves the temperature increases from top to bottom when $\lambda < \lambda_c$.

extrapolating to $kT = 0$.

When $\gamma = 0.5$ (anisotropic XY model) and $\gamma = 1.0$ (Ising transverse model), the QCP is determined, respectively, by the inflection points of $\overline{\mathcal{F}}$ and $d\overline{\mathcal{F}}/d\lambda$ that occur exactly at $\lambda_c = 1.0$ when $T = 0$ (see Figs. 8 and 9). For higher values of T , the inflection points are displaced away from λ_c and the best strategy to estimate the QCP is by determining the location of the maximum (minimum) of the second order derivatives of $\overline{\mathcal{F}}$ with respect to λ . The location of these extremum values lie close to λ_c when $kT \lesssim 0.1$ and, as we will show below, by extrapolating to the absolute zero temperature we can predict its correct value. Note also that the one- and two-point correlation functions have inflection points at the QCP when $T = 0$ [26].

In Figs. 10, 11, and 12 we plot the minimum mean trace distance $\overline{\mathcal{D}}$ as a function of λ for the same three values of γ and temperatures shown in Figs. 7 to 9. Looking at Figs. 7 to 12, and taking into account that a high value for $\overline{\mathcal{F}}$ implies a low value for $\overline{\mathcal{D}}$, we realize that the behavior of $\overline{\mathcal{F}}$ and $\overline{\mathcal{D}}$ about the QCPs are very similar for a given value of γ .

Similarly to the behavior of $\overline{\mathcal{F}}$ at $T = 0$, for the isotropic XX model ($\gamma = 0.0$) the QCP is identified by a discontinuity in the derivative of $\overline{\mathcal{D}}$ with respect to λ at λ_c (see Fig. 10). For $T > 0$, we no longer have a discontinuity in the derivative of $\overline{\mathcal{D}}$ but rather a high value for its magnitude about the QCP. The location of this extremum moves away from the exact value of the QCP as we increase T . For $kT \lesssim 0.1$, though, these extrema are near to the correct value of the QCP and we will show in what follows how to use these finite T data to extract the exact location of the QCP.

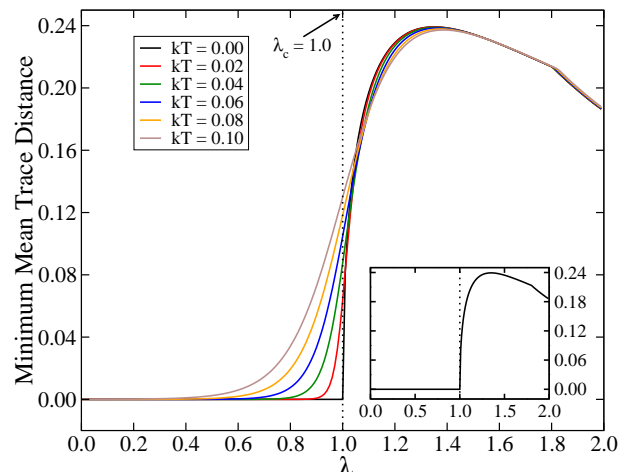
XY model with $\gamma = 0.0$ 

FIG. 10: (color online) $\overline{\mathcal{D}}$, Eq. (45), as a function of λ for several values of kT while fixing $\gamma = 0.0$ (XX model in a transverse field). The inset shows the $T = 0$ curve and the dotted lines mark the QCP λ_c . For the solid curves the temperature decreases from top to bottom when $\lambda < \lambda_c$.

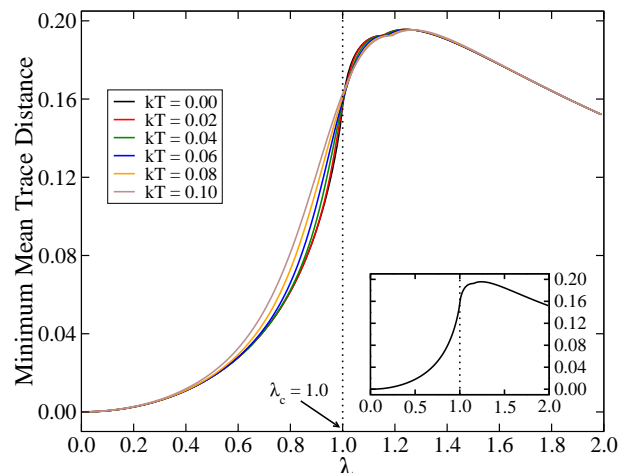
XY model with $\gamma = 0.5$ 

FIG. 11: (color online) Same as Fig. 10 but now $\gamma = 0.5$. The inset shows the $T = 0$ curve and the dotted lines mark the QCP λ_c . For the solid curves the temperature decreases from top to bottom when $\lambda < \lambda_c$.

The same qualitative features observed for the behavior of $\overline{\mathcal{F}}$ as a function of λ can be seen for $\overline{\mathcal{D}}$ when we work with $\gamma = 0.5$ (anisotropic XY model) and $\gamma = 1.0$ (Ising transverse model). Again, at $T = 0$ the critical point λ_c is given, respectively, by an inflection point of $\overline{\mathcal{D}}$ and of $d\overline{\mathcal{D}}/d\lambda$ at $\lambda_c = 1.0$ (see Figs. 11 and 12). If we increase T , though, the inflection points move away from $\lambda_c = 1.0$. As we will see, using finite T data we can best estimate the correct value for λ_c by computing the location of the extremum values of the second order

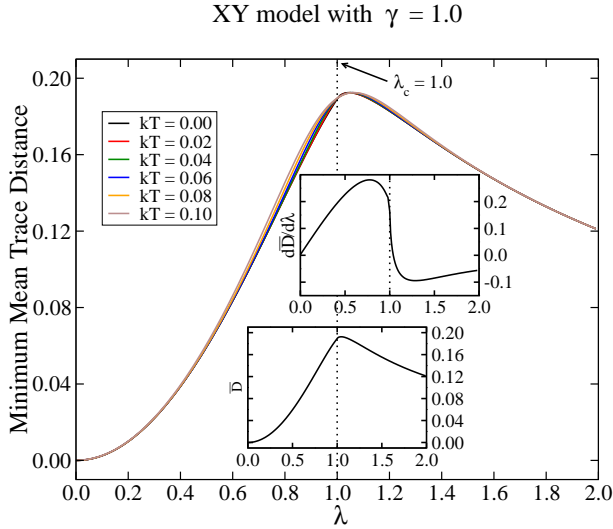


FIG. 12: (color online) Same as Fig. 10 but now $\gamma = 1.0$ (Ising model in a transverse field). The lower inset highlights the $T = 0$ curve of \overline{D} and the upper inset its derivative with respect to λ . The dotted lines mark the QCP λ_c . For the solid curves the temperature decreases from top to bottom when $\lambda < \lambda_c$.

derivatives of \overline{D} with respect to λ and then numerically taking the $T = 0$ limit.

Let us show now how to determine the QCPs using finite T data. Following the strategy outlined in Sec. III, for several values of temperature we numerically evaluate the first and second order derivatives with respect to λ of \overline{D} , \overline{F} , and of the one- and two-point correlation functions. Then, we employ the location of the extrema of those derivatives as the value for the QCP. When $\gamma = 0.0$, the location of the maximum of the first order derivative of \overline{D} is the optimal strategy to obtain the correct value for λ_c (see Fig. 13). Indeed, for all values of temperature up to $kT = 0.1$, the predicted value for λ_c lies within the correct $T = 0$ value ($\lambda_c = 1.0$) if we take into account, as explained in Sec. III, the uncertainties (± 0.01) in obtaining the spot of the maximum of $d\overline{D}/d\lambda$.

If we now fix $\gamma = 0.5$, the extrema of $d^2\overline{F}/d\lambda^2$ lie closer to the true value of the QCP than those of $d^2\overline{D}/d\lambda^2$ when $kT > 0.02$ (see Fig. 14). For high values of kT , the extrema of $d(xx)/d\lambda$ are the optimal choice to estimate the QCP and, as we keep decreasing T , all quantities eventually give the exact location for the QCP. It is worth noting that if we take into account the errors (yellow-shaded regions in Fig. 14) in numerically locating the extrema of $d^2\overline{F}/d\lambda^2$, for all temperatures shown in Fig. 14 the exact value of the QCP lies within the range of possible values for the location of those extrema.

When $\gamma = 1.0$, we realize looking at Fig. 15 that up to $kT = 0.03$ the extrema of $d(yy)/d\lambda$ and $d^2\overline{D}/d\lambda^2$ give the correct value for the QCP. And if we take into account the errors in numerically estimating the extrema of $d^2\overline{D}/d\lambda^2$, both quantities are almost equally optimal in predicting the correct value of the QCP for higher values of kT (see

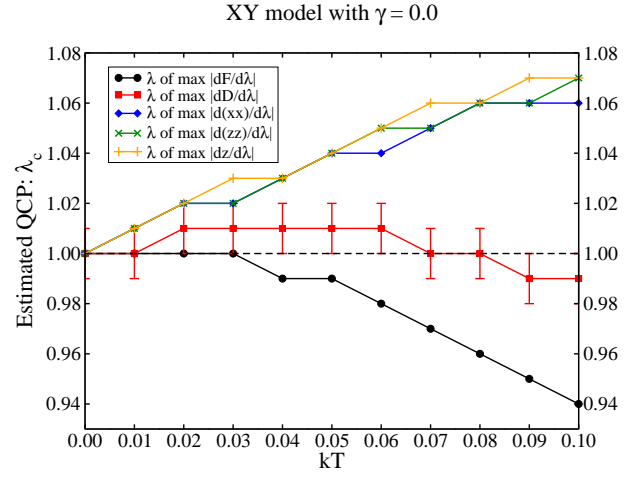


FIG. 13: (color online) Estimated value for the critical point λ_c using finite T data. The locations of the maxima of the first order derivatives of \overline{D} with respect to λ for several values of T best approximate the correct location of the QCP (red-square curve). The error bars depict the uncertainties in numerically obtaining the location of the maxima of $d\overline{D}/d\lambda$. The dashed line gives the exact value of the QCP and the other solid curves give the locations of the extrema of the first order derivatives of \overline{F} and of the one- and two-point correlation functions. For ease of visualization, we do not show the error bars in these cases. See text for details.

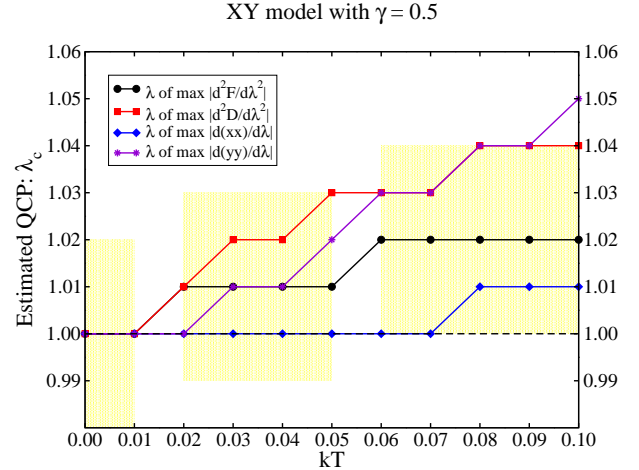


FIG. 14: (color online) Same as Fig. 13. The yellow-shaded regions represent the uncertainty in the numerical determination of the locations of the extrema for the second derivatives of \overline{F} (± 0.02). For ease of visualization, we do not show the errors associated with the other quantities and we do not show the curves and points giving the locations of the extrema of $dz/d\lambda$ and $d(zz)/d\lambda$. The latter curves lie between the curves above depicting the locations of the extrema for $d(yy)/d\lambda$ and $d(xx)/d\lambda$.

Fig. 15).

We can be more quantitative in the prediction of the location of the QCP by following the same strategy of Ref. [26] that was already explained in Sec. III. For all

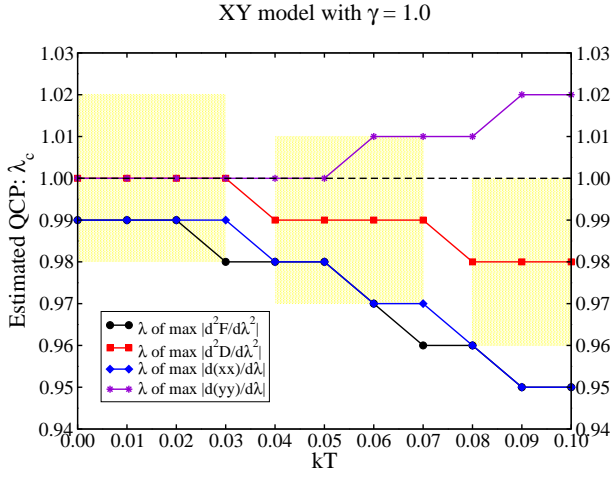


FIG. 15: (color online) Same as Fig. 13. The yellow-shaded regions represent the uncertainty in the numerical determination of the locations of the extrema for the second derivatives of \overline{D} (± 0.02). For ease of visualization, we do not show the errors associated with the other quantities and we do not show the locations of the extrema of $dz/d\lambda$ and $d(zz)/d\lambda$, which lie between the curves above showing the locations of the extrema for $d(yy)/d\lambda$ and $d(xx)/d\lambda$.

the quantities shown in Figs. 13 to 15, we excluded the $kT = 0.0$ point and implemented a linear regression with the remaining data ($kT = 0.01, 0.02, \dots, 0.10$). Using the fitted curves, we took the $kT = 0$ limit and obtained for all cases and within the numerical errors already reported the correct value for the QCP.

A closer look at the curves for \overline{D}

Before we move to the study of the anisotropy transition, it is important to better analyze the behavior of the minimum mean trace distance \overline{D} as a function of λ (a similar analysis applies to \overline{F} as well). Looking at Fig. 10, where we fixed $\gamma = 0.0$, we note a cusp located about $\lambda = 1.8$ that is not associated with a QPT. The origin of this cusp can be traced back to the point where the function minimizing \overline{D} , namely, $\overline{D}(S_{\Phi\pm})$, is replaced by $\overline{D}(S_{\Psi\pm})$. This is illustrated in Fig. 16, where we can also understand the cusp seen at $\lambda \approx 1.5$ for \overline{F} in Fig. 7. This is the point where $\overline{F}(S_{\Psi\pm}) = \overline{F}(S_{\Phi\pm})$. Before this point \overline{F} is given by $\overline{F}(S_{\Phi\pm})$ and after it by $\overline{F}(S_{\Psi\pm})$.

Plotting the same curves for $\gamma = 0.5$ and $\gamma = 1.0$, we realize that the mean fidelity curves as well as the mean trace distance ones do not cross each other. This is why we do not have a cusp in Figs. 8 and 9 and also in Fig. 12. We do have a small cusp, though, for the curves of \overline{D} given in Fig. 11, where we fixed $\gamma = 0.5$. This cusp is not related to a QPT and we can understand its origin by carefully looking at the functional form of $\overline{D}(S_{\Phi\pm})$, which gives the minimum mean trace distance \overline{D} when $0 \leq \lambda \leq 2$ (see Fig. 17).

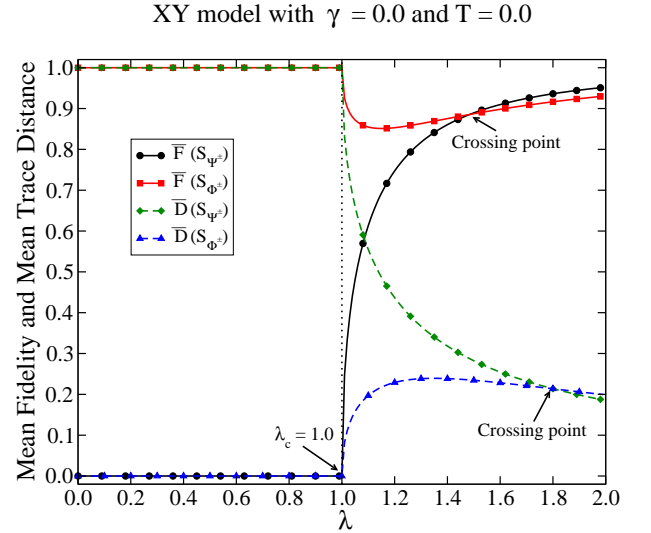


FIG. 16: (color online) Mean fidelities $\overline{F}(S_{\Psi\pm})$ and $\overline{F}(S_{\Phi\pm})$ [Eqs. (38) and (39)] and mean trace distances $\overline{D}(S_{\Psi\pm})$ and $\overline{D}(S_{\Phi\pm})$ [Eqs. (43) and (44)] as a function of λ when $kT = 0$ and $\gamma = 0.0$ (XX model in a transverse field). The highlighted points, which we called “crossing points”, are located exactly at the cusps of \overline{F} and \overline{D} seen in Figs. 7 and 10, respectively. Note that these cusps are not related to QPTs and they move to higher values of λ as we increase the temperature.

Looking at Eq. (44), we note that the second term defining $\overline{D}(S_{\Phi\pm})$ is $|z^3 - z \cdot zz|$. Studying the sign of $z^3 - z \cdot zz$, we realize that before the cusp seen in Fig. 11 we have $z^3 - z \cdot zz < 0$ while after it we have $z^3 - z \cdot zz > 0$. The change of sign of $z^3 - z \cdot zz$ leads to a discontinuity in the derivative of $\overline{D}(S_{\Phi\pm})$ with respect to λ and this gives rise to the cusp seen in Fig. 11. When $\gamma = 1.0$, however, we have $z^3 - z \cdot zz \leq 0$ when $0.0 \leq \lambda \leq 2.0$ and this is why we do not see a similar cusp in Fig. 12.

Studying the behavior of $z^3 - z \cdot zz$ and of z , specifically their sign for $0.0 \leq \lambda \leq 2.0$, we can simplify the expressions for \overline{D} within that range of values for λ . When $\gamma = 0$, we have $z^3 - z \cdot zz \geq 0$ and $z > 0$ [26]. Thus, Eq. (45) becomes

$$\overline{D}_{\gamma=0} = \begin{cases} z(1 - zz)/2, & \text{if } zz \geq -z^2, \\ z(1 + z^2)/2, & \text{if } zz \leq -z^2. \end{cases} \quad (56)$$

Note that the condition $zz = -z^2$ is the solution to $\overline{D}(S_{\Phi\pm}) = \overline{D}(S_{\Psi\pm})$, which determines one of the crossing points shown in Fig. 16.

If we now set $\gamma = 0.5$, we have that \overline{D} is always given by $\overline{D}(S_{\Phi\pm})$ (cf. Fig. 17). We also have for $0.0 \leq \lambda \leq 2.0$ that $z > 0$ [26]. Noting that in this scenario $z^3 - z \cdot zz$ changes sign at $zz = z^2$, we obtain for Eq. (45),

$$\overline{D}_{\gamma=0.5} = \begin{cases} z(1 - z^2)/2, & \text{if } zz \geq z^2, \\ z(1 - zz)/2, & \text{if } zz \leq z^2. \end{cases} \quad (57)$$

When $\gamma = 1.0$ and $0.0 \leq \lambda \leq 2.0$, we also have $z > 0$ [26] and \overline{D} given by $\overline{D}(S_{\Phi\pm})$ (cf. Fig. 18). In this case,

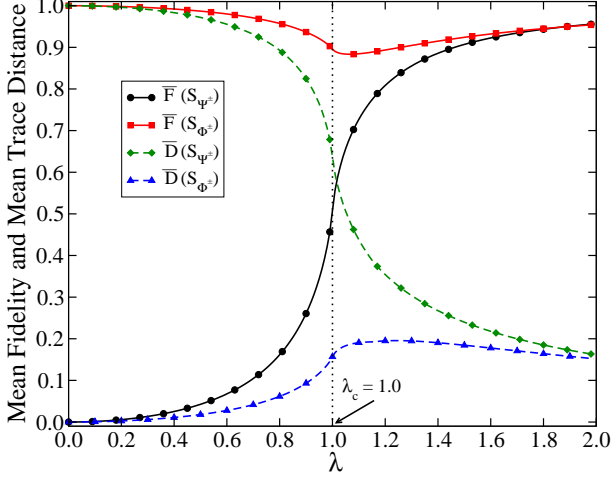
XY model with $\gamma = 0.5$ and $T = 0.0$ 

FIG. 17: (color online) Same as Fig. 16 but now we have $\gamma = 0.5$ (anisotropic XY model in a transverse field). Note that the solid curves do not cross each other. The same applies to the dashed ones.

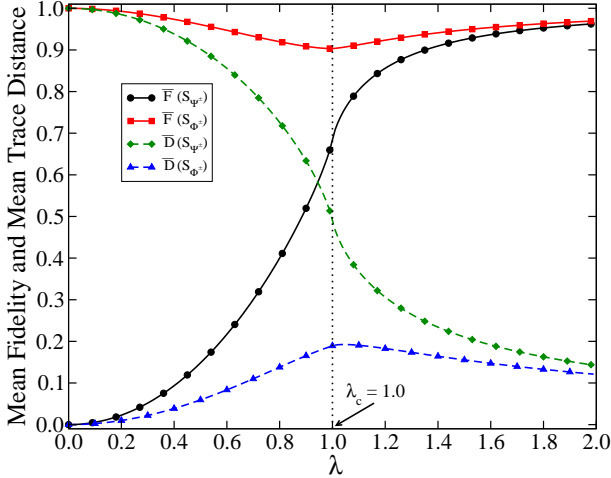
XY model with $\gamma = 1.0$ and $T = 0.0$ 

FIG. 18: (color online) Same as Fig. 17 but now we have $\gamma = 1.0$ (Ising transverse model).

though, we always get that $z^3 - z \cdot zz \leq 0$. Therefore,

$$\bar{D}_{\gamma=1.0} = z(1 - z^2)/2. \quad (58)$$

B. The γ transition

In Figs. 19 and 20 we plot, respectively, \bar{F} and \bar{D} as functions of γ while fixing $\lambda = 1.5$.

Looking at Fig. 19, we note that the QCP located at $\gamma_c = 0.0$ is given by the global minimum of \bar{F} , which occur exactly at γ_c even for finite T . If we now look at Fig. 20, we realize that the global maximum of \bar{D} marks

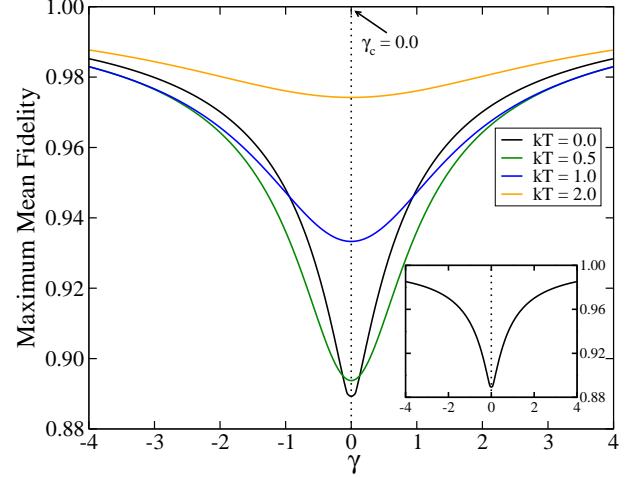
XY model with $\lambda = 1.5$ 

FIG. 19: (color online) \bar{F} , Eq. (42), as a function of γ with $\lambda = 1.5$ [see Eq. (55)]. At $T = 0$ and $T > 0$, the QCP $\gamma_c = 0.0$ is detected by a minimum that occurs at the exact location of the QCP. The dotted lines spotlight the QCP γ_c and for the solid curves the temperature increases from bottom to top along the dashed line.

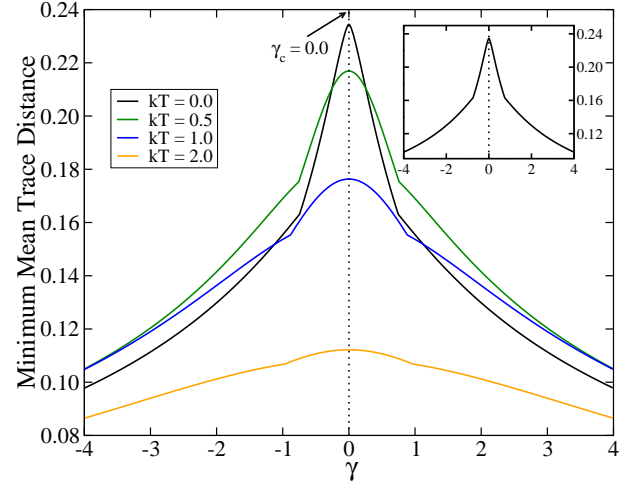
XY model with $\lambda = 1.5$ 

FIG. 20: (color online) Same as Fig. 19 but now we have \bar{D} , Eq. (45), as a function of γ . In this case the QCP is detected by a cusp at $T = 0$ (see inset), with the latter being smoothed out as we increase kT . For the solid curves, the temperature increases from top to bottom along the dashed line.

the location of the QCP. At $T = 0$ we also have a cusp at the maximum, which is smoothed out as we increase T . However, the maximum of \bar{D} is not displaced as we increase T , being always situated at the exact location of the QCP. There are two other cusps in the curve for \bar{D} that are not related to QPTs. They occur when $z^3 - z \cdot zz$ changes sign. Before the first cusp and after the last cusp we have $z^3 - z \cdot zz < 0$ while between those cusps we have $z^3 - z \cdot zz > 0$. Since \bar{D} depends on the magnitude of

$z^3 - z \cdot zz$, these sign changes lead to two discontinuities of $d\overline{\mathcal{D}}/d\gamma$ as we vary γ . These discontinuities in the derivatives of $\overline{\mathcal{D}}$ manifest themselves as two cusps in the curves for $\overline{\mathcal{D}}$ that are not related to QPTs.

The robustness of $\overline{\mathcal{D}}$ to spotlight the anisotropy transition as we increase T can be understood by noting three things that are simultaneously true in the neighborhood of the QCP for all the values of temperature shown in Fig. 20. By the neighborhood of the QCP we mean the region between the two cusps depicted in Fig. 20 that are not related to QPTs.

First, in the neighborhood of the QCP we have that $\overline{\mathcal{D}} = \overline{\mathcal{D}}(S_{\Phi\pm})$. Second, $z > 0$ and $z^3 - z \cdot zz \geq 0$. Third, z has a maximum at γ_c while zz has a minimum there [26]. The first two facts imply that

$$\overline{\mathcal{D}}_{\lambda=1.5} = z(1 - zz)/2, \text{ if } zz \leq z^2. \quad (59)$$

The third fact gives $\dot{z} = \dot{zz} = 0$, $\ddot{z} < 0$, and $\ddot{zz} > 0$ at γ_c , where the single and double dots denote the first and second order derivatives with respect to γ . A simple calculation using Eq. (59) and the derivatives above give at γ_c ,

$$\frac{d}{d\gamma} \overline{\mathcal{D}}_{\lambda=1.5}(\gamma_c) = 0, \quad (60)$$

$$\frac{d^2}{d\gamma^2} \overline{\mathcal{D}}_{\lambda=1.5}(\gamma_c) = \frac{\ddot{z}(1 - zz) - z \cdot \ddot{zz}}{2} < 0, \quad (61)$$

where the last inequality comes from the fact that $\ddot{z} < 0$, $|zz| \leq 1$, $z > 0$, and $\ddot{zz} > 0$. In other words, $\overline{\mathcal{D}}$ has always a maximum at the QCP for all the values of temperature given in Fig. 20.

Remark 8: A similar analysis explains why the maximum mean fidelity $\overline{\mathcal{F}}$ has a minimum at the QCP for all the temperatures shown in Fig. 19.

V. DISCUSSION

The strategy developed in this work to detect quantum critical points (QCPs) using finite temperature data simplifies the teleportation based QCP detectors first given in Ref. [26]. In Ref. [26], the state to be teleported to one of the qubits of the spin chain was external to it. Here, however, we showed that by using an internal qubit, i.e., a qubit that belongs to the chain itself, we can still detect QCPs with finite T data using the same techniques of Ref. [26] if we have spin chains embedded in an external magnetic field. In this scenario and for all spin chain models studied here, we showed that the efficiency of the teleportation protocol or its derivative change drastically at a QCP.

The present proposal also retains the remarkable features of the former one [26]. From a theoretical point of view, all we need to calculate the efficiency of the teleportation protocol, quantified by either the maximum mean fidelity $\overline{\mathcal{F}}$ or the minimum mean trace distance $\overline{\mathcal{D}}$, is the state describing two nearest neighbor qubits of the

spin chain [Eq. (20)], with the latter assumed to be in equilibrium with a heat bath at temperature T . This two-qubit density matrix is theoretically computed by tracing out all but these two nearest neighbors from the canonical ensemble density matrix describing the complete chain. Equivalently, if we are able to compute all the one- and two-point correlation functions we can determine the two-qubit density matrix describing a pair of spins since it is completely characterized by these correlation functions.

The standard approach to study quantum phase transitions also makes use of those correlation functions or of quantities that depend on them (the magnetic susceptibility, for instance). The QCPs are detected at $T = 0$ by discontinuities in the n -th order derivatives of those quantities at the QCPs. Quantum information theory quantities, such as bipartite or multipartite entanglement and quantum discord, are useful to spotlight QCPs too [7–12, 20, 21]. See also the application of generalized phase-space techniques to detect QCPs [53, 54]. All these quantities are functions of the correlation functions of the system, the same ones we need to theoretically apply the present and the method of Ref. [26].

As already pointed out in Ref. [26], some of the standard quantities used to detect QCPs (magnetization or magnetic susceptibility, for instance) become less effective to correctly identify the QCPs with finite T data [21]. And some quantum information theory quantities, in particular the entanglement of formation [19], are zero at and around the QCPs as we increase T . These quantities cannot be employed to spotlight QCPs after a certain temperature threshold [21]. On the other hand, a specific measure of non-classical correlations between two systems, namely, quantum discord [22, 23], is extremely robust to spotlight QCPs at finite T [21]. The present internal teleportation based tools to detect QCPs as well as the ones of Ref. [26] share the quantum discord robustness to detect QCPs with finite T data.² In addition to that, and contrary to quantum discord, the present tools and the ones of Ref. [26] do not become computationally intractable if we deal with high spin systems (high dimensional Hilbert spaces) [26].

Turning our attention to the experimental aspects of the present proposal, it is clearly simpler than the external teleportation QCP detector tools [26]. There is no need to bring a qubit outside from the spin chain to implement the present proposal. The input state to be teleported belongs to the chain itself. Indeed, contrary to the external teleportation QCP detector, there is no need to repeat the protocol with many different input

² Note that it is important to analyze the $T = 0$ limit from the finite T data to make sure that no spurious classical critical point is “contaminating” the finite T data. Only if the finite T data consistently tend to a specific critical point as we decrease T can we be reassured that we are properly seeing a QCP. See, for instance, Figs. 6, 13, 14, and 15.

qubits that cover the whole Bloch sphere [26]. For the internal teleportation QCP detector, the input state is fixed and belongs to the system under study. Also, the present scheme and that of Ref. [26] have a straightforward experimental interpretation since they are built on the quantum teleportation protocol. Quantum discord, though, has no direct experimental procedure to its determination.

To execute the internal teleportation protocol, and thus the present proposal, we need to be able to implement single qubit measurements, Bell state measurements, and local unitary operations on the qubits that belong to a spin chain. The single qubit measurement we need is a projective measurement onto the eigenstates of the σ^z observable (our computational basis). A Bell state measurement is a joint measurement involving two qubits that aims to project the two qubits onto one of the four Bell states. This measurement can be divided into the following sequence of three steps [35]. First, we implement a controlled-NOT (CNOT) gate on the pair of spins we will be measuring, now called control and target qubits. The CNOT is a two-qubit (non-local) gate whose “truth table” in the standard basis is such that it flips the spin of the target qubit if, and only if, the control qubit is given by $|1\rangle$. The standard basis can be, for instance, the eigenstates of the spin operator σ^z . Second, we implement a Hadamard gate on the control qubit of the CNOT gate. This is a single (local) qubit gate whose truth table is $(|0\rangle + (-)|1\rangle)/\sqrt{2} \rightarrow |0\rangle(|1\rangle)$. Third, we measure the two qubits in the standard (computational) basis $\{|00\rangle, |01\rangle, |10\rangle, |11\rangle\}$. Each one of the four previous outcomes in the standard basis implies that we projected the two qubits onto one of the four Bell states [35]. The single qubit and Bell measurements are Alice’s job while Bob’s job is to measure his qubit after implementing the appropriate local operation (local gate) as given by Eqs. (8)-(11). All these gates, the ones needed by Alice and Bob, are already being implemented in spin chain-like systems using state of the art techniques [55–61]. We believe that in the near future they can be implemented in the sequence described above to execute the teleportation protocol and consequently the present proposal. We should remark that the experiments reported in Refs. [55–61] were done using small systems. However, some of them implemented efficiently the one- and two-qubit gates at room temperature.

Furthermore, using superconducting qubits to realize a spin chain, it is already possible to experimentally prepare tens of spins simultaneously with coherence times around $100\mu s$. Also, single and two-qubit gates in this platform can be implemented within $10ns$ to $100ns$, leading to the execution of 10^3 to 10^4 gates per coherence time [62]. We can also implement spin chains experimentally using quantum dots and wells. For quantum wells built with GaAs, at room temperature the relaxation time is of the order of a few nanoseconds [63]. And for GaAs quantum dots, the relaxation time for a qubit is about $50\mu s$ at $T \approx 20mK$ [64] while for arrays of Ge/Si quan-

tum dots we have a relaxation time of about $10\mu s$ at $T \approx 5K$ [65]. These facts, together with the fact that in silicon quantum dots at $T \approx 1K$ we can implement single and two-qubit gates in less than $100ns$ [66], imply that at low temperatures ($\approx 1K$) and for silicon quantum dots it is possible to execute one hundred or so gates before the spin chain thermalizes. This number of gates is at least one order of magnitude more than what we need to implement the present proposal, where only a few gates (fewer than ten) are needed at a given run of the teleportation protocol.³

Note that the time span to execute all the steps of the teleportation protocol plus Bob’s measurement of the teleported qubit should not exceed the “relaxation time” of the spin chain. That is, all the steps should be performed before the spin chain returns to its equilibrium state with the heat bath. This equilibration time depends on the system’s Hamiltonian, its initial state, and how it interacts with the heat bath. Its theoretical computation is very challenging, lying beyond the scope of the present work. Experimentally, it can be determined by perturbing the system appropriately using the above gates and measuring how long it takes to return to its equilibrium state.

We should also contrast the present proposal with the standard way of studying QPTs from the experimental point of view. In the standard way, we must measure the one- and two-point correlation functions using, for instance, neutron scattering techniques. The non-analytic properties of these one- and two-point correlation functions at the QCP mark a QPT. In the present proposal, we need only to measure one-point correlation functions after “disturbing” the system in a specific way. Indeed, to reconstruct the state describing his qubit after the teleportation protocol (the “disturbance” in the spin chain), Bob only needs one-point correlation functions. Any single qubit density matrix is completely characterized once we know all the one-point correlation functions $\langle\sigma^x\rangle$, $\langle\sigma^y\rangle$, and $\langle\sigma^z\rangle$ [35]. And in all the models investigated here, we only need one correlation function, $\langle\sigma^z\rangle$ to be specific. This is true since the qubit with Bob after the teleportation protocol is diagonal in the standard basis [see Eqs. (46)-(49)]. In other words, we are trading the measurement of two-point correlation functions to experimentally determine a QCP for the measurement of only one one-point correlation function after disturbing the system in a very particular way, namely, after applying all the gates associated with the internal quantum

³ The quantum circuit representing all the steps of the teleportation protocol can be seen in Ref. [35] while a review on thermalization is given in Ref. [67]. See also Ref. [68] for a quantum circuit realization of a heat bath in solid quantum systems. Furthermore, with the advent of a quantum computer, it will be possible to efficiently simulate and even prepare thermal states [69–72], which in turn can be used to implement the present QCP detection strategy.

teleportation protocol.

Finally, we want to emphasize that the previous paragraph in no way implies that the present proposal is experimentally simpler or easier than the standard approach to detect QCP, namely, the direct measurement of one- and two-point correlation functions. Actually, the internal teleportation based QCP detector can be applied to detect a QCP whether or not it is experimentally implemented as described in the previous paragraphs. The same standard experimental techniques to measure one- and two-point correlation functions serve as well. Once we have those correlation functions, we automatically obtain Eq. (20), from which the maximal mean fidelity $\overline{\mathcal{F}}$ and the minimum mean trace distance $\overline{\mathcal{D}}$ associated with the internal teleportation based QCP detector can be computed. And if we look at Eqs. (42) and (45), we realize that it is the non-linear dependence of $\overline{\mathcal{F}}$ and $\overline{\mathcal{D}}$ on the one- and two-point correlation functions that sets them apart from the external teleportation QCP detector, where the fidelity is a simple linear function of a specific two-point correlation function. We believe that this unique functional form of $\overline{\mathcal{F}}$ and $\overline{\mathcal{D}}$ is the reason of why the internal teleportation QCP detector outperforms the external one most of the time.

VI. CONCLUSION

We simplified the teleportation based quantum critical point (QCP) detector of Ref. [26] in a very important way, reducing the technical demands to its possible experimental realization. Instead of using an external qubit from the spin chain as the input state to be teleported to the chain, in this work we employed a qubit within the spin chain itself. Several spin-1/2 chain models in the thermodynamic limit were used to test the efficacy of this new approach in detecting a QCP at zero and non-zero temperatures. We showed that whenever the spin chain is immersed in an external magnetic field, the present “internal” teleportation based QCP detector retains all the remarkable characteristics of the “external” teleportation based QCP detector of Ref. [26]. In particular, we showed that the present strategy detects the QCPs for the XXZ model in a longitudinal field, the Ising transverse model, the isotropic XX model in a transverse field, and the anisotropic XY model in a transverse field. Note that we worked with these models because their QCPs were previously characterized by other methods. In this way we could properly compare the predicted location for the QCPs coming from the present tool with the well-known and established locations for those QCPs.

The main idea behind the present and the proposal of Ref. [26] is to use a pair of qubits from the spin chain as the entangled resource shared between Alice and Bob in the implementation of the teleportation protocol. In this work, an internal qubit of the chain, adjacent to the pair of qubits shared between Alice and Bob, is teleported to Bob. Similarly to what we saw in Ref. [26], we proved

that the efficiency of the teleportation protocol changes considerably as we cross the QCP. In other words, the efficiency of the teleportation protocol depends on the quantum phase in which the spin chain lies. The efficiency of the teleportation protocol in this work was quantified by using both the fidelity and the trace distance between the input and output states, namely, between Alice’s input state and Bob’s final qubit at the end of the teleportation protocol.

For the several models investigated here, we observed that at $T = 0$ the maximum mean fidelity $\overline{\mathcal{F}}$ and the minimum mean trace distance $\overline{\mathcal{D}}$ between the teleported and the input states possess a cusp or an inflection point exactly at the QCPs. When we increase T , these cusps are smoothed out and both the cusps and the inflection points are displaced from the exact locations of the QCPs. At finite temperatures, these cusps and inflection points manifest themselves in a high value for the magnitudes of the first and second order derivatives of $\overline{\mathcal{F}}$ and $\overline{\mathcal{D}}$ around the exact locations of the QCPs. We also showed that for small values of temperature, the extrema of these derivatives lie close together and by taking the zero temperature limit we are able to correctly predict the $T = 0$ location of the QCP.

Furthermore, the internal teleportation based QCP detector shares the same features of the external one and of the quantum discord, when the latter is also employed as a tool to detect QCPs [21]. These tools can be used without the knowledge of the order parameter associated with the quantum phase transition being investigated and they are very resilient to the increase of temperature, giving us useful information at finite T that allows us to predict the exact value of the QCP at $T = 0$. On top of that, and contrary to the quantum discord, the QCP detectors here developed and in Ref. [26] have a straightforward experimental meaning and are scalable to high spin systems [26].

We want to end this work by calling attention to a feature already highlighted in Ref. [26] and that is also observed here. This feature is related to the fact that for each model investigated in this work we have a distinctive functional form for $\overline{\mathcal{F}}$ and $\overline{\mathcal{D}}$. For some models we have extra cusps for these functions that are not related to a quantum phase transition, for other models the QCP is detected via an inflection point of $\overline{\mathcal{F}}$ and $\overline{\mathcal{D}}$, and for others we have the QCP being detected by discontinuities in their derivatives. Putting it differently, the “fingerprint” of a quantum phase, a quantum phase transition, and the underlying model dictating these phases and transitions are unique. The functional forms of $\overline{\mathcal{F}}$ and $\overline{\mathcal{D}}$ as we drive the system around its phase space are specific for a given model. A systematic study $\overline{\mathcal{F}}$ and $\overline{\mathcal{D}}$ enables the proper detection of the QCP using finite T data and, interestingly, also the discovery of the underlying spin chain model giving rise to those quantum phases and quantum phase transitions.

We should also remark that the above features are still present for spin chains away from the thermodynamic

limit. Preliminary calculations using spin chains containing about 10 qubits already show that we can detect the QCPs with reasonable accuracy and using finite temperature data only [73]. Moreover, in order to properly exclude finite size effects or spurious discontinuities in the derivatives of \overline{F} and \overline{D} that are not related to QCPs, both the external and internal teleportation based QCP detectors must be used [73]. Only discontinuities in the derivatives that occur in both quantities at the same place are the ones marking a QCP. Spurious discontinuities or finite size effects not related to a QCP do not occur at the same spot in both quantities [73]. In other words, the internal teleportation QCP detector not only behaves differently from the external one but it is crucial in the task of identifying finite size effects or spurious dis-

continuities in the fidelity and in the trace distance that are not associated with QCPs.

Acknowledgments

GR thanks the Brazilian agency CNPq (National Council for Scientific and Technological Development) for funding and CNPq/FAPERJ (State of Rio de Janeiro Research Foundation) for financial support through the National Institute of Science and Technology for Quantum Information. GAPR thanks the São Paulo Research Foundation (FAPESP) for financial support through the grant 2023/03947-0.

-
- [1] S. Sachdev, *Quantum Phase Transitions* (Cambridge University Press, Cambridge, 1999).
- [2] M. Greiner, O. Mandel, T. Esslinger, T. W. Hänsch, and I. Bloch, *Nature (London)* **415**, 39 (2002).
- [3] V. F. Gantmakher and V. T. Dolgoplov, *Phys. Usp.* **53**, 1 (2010).
- [4] S. Rowley, R. Smith, M. Dean, L. Spalek, M. Sutherland, M. Saxena, P. Alireza, C. Ko, C. Liu, E. Pugh *et al.*, *Phys. Status Solidi B* **247**, 469 (2010).
- [5] A. Osterloh, L. Amico, G. Falci, and R. Fazio, *Nature (London)* **416**, 608 (2002).
- [6] T. J. Osborne and M. A. Nielsen, *Phys. Rev. A* **66**, 032110 (2002).
- [7] L.-A. Wu, M. S. Sarandy, and D. A. Lidar, *Phys. Rev. Lett.* **93**, 250404 (2004).
- [8] T. R. de Oliveira, G. Rigolin, M. C. de Oliveira, and E. Miranda, *Phys. Rev. Lett.* **97**, 170401 (2006); T. R. de Oliveira, G. Rigolin, and M. C. de Oliveira, *Phys. Rev. A* **73**, 010305 (2006); T. R. de Oliveira, G. Rigolin, M. C. de Oliveira, and E. Miranda, *Phys. Rev. A* **77**, 032325(R) (2008).
- [9] R. Dillenschneider, *Phys. Rev. B* **78**, 224413 (2008).
- [10] M. S. Sarandy, *Phys. Rev. A* **80**, 022108 (2009).
- [11] G. Karpat, B. Çakmak, and F. F. Fanchini, *Phys. Rev. B* **90**, 104431 (2014).
- [12] D. Girolami, *Phys. Rev. Lett.* **113**, 170401 (2014).
- [13] M. Hotta, *Phys. Lett. A* **372**, 5671 (2008).
- [14] M. Hotta, *J. Phys. Soc. Jpn.* **78**, 034001 (2009).
- [15] K. Ikeda, *Phys. Rev. D* **107**, L071502 (2023).
- [16] K. Ikeda, *Phys. Rev. Appl.* **20**, 024051 (2023).
- [17] K. Ikeda, *AVS Quantum Sci.* **5**, 035002 (2023).
- [18] K. Ikeda, R. Singh, and R.-J. Slager, e-print arXiv:2310.15936 [quant-ph].
- [19] W. K. Wootters, *Phys. Rev. Lett.* **80**, 2245 (1998).
- [20] T. Werlang and G. Rigolin, *Phys. Rev. A* **81**, 044101 (2010).
- [21] T. Werlang, C. Trippe, G. A. P. Ribeiro, and G. Rigolin, *Phys. Rev. Lett.* **105**, 095702 (2010); T. Werlang, G. A. P. Ribeiro, and G. Rigolin, *Phys. Rev. A* **83**, 062334 (2011); T. Werlang, G. A. P. Ribeiro, and G. Rigolin, *Int. J. Mod. Phys. B* **27**, 1345032 (2013).
- [22] H. Ollivier and W. H. Zurek, *Phys. Rev. Lett.* **88**, 017901 (2001).
- [23] L. Henderson and V. Vedral, *J. Phys. A: Math. Gen.* **34**, 6899 (2001).
- [24] Y. Huang, *New J. Phys.* **16**, 033027 (2014).
- [25] A. L. Malvezzi, G. Karpat, B. Çakmak, F. F. Fanchini, T. Debarba, and R. O. Vianna, *Phys. Rev. B* **93**, 184428 (2016).
- [26] G. A. P. Ribeiro and G. Rigolin, *Phys. Rev. A* **107**, 052420 (2023); G. A. P. Ribeiro and G. Rigolin, *Phys. Rev. A* **109**, 012612 (2024).
- [27] C. H. Bennett, G. Brassard, C. Crepeau, R. Jozsa, A. Peres, and W. K. Wootters, *Phys. Rev. Lett.* **70**, 1895 (1993).
- [28] Y. Yeo, *Phys. Rev. A* **66**, 062312 (2002).
- [29] R. Fortes and G. Rigolin, *Phys. Rev. A* **96**, 022315 (2017).
- [30] L. C. Venuti, C. D. E. Boschi, and M. Roncaglia, *Phys. Rev. Lett.* **96**, 247206 (2006).
- [31] L. C. Venuti, S. M. Giampaolo, F. Illuminati, and P. Zanardi, *Phys. Rev. A* **76**, 052328 (2007).
- [32] L. C. Venuti, C. D. E. Boschi, and M. Roncaglia, *Phys. Rev. Lett.* **99**, 060401 (2007).
- [33] S. Abaach, Z. Mzaouali, and M. El Baz, *Sci. Rep* **13**, 964 (2023).
- [34] R. Fortes and G. Rigolin, *Phys. Rev. A* **92**, 012338 (2015); **93**, 062330 (2016).
- [35] M. A. Nielsen and I. L. Chuang, *Quantum Computation and Quantum Information* (Cambridge University Press, Cambridge, 2000).
- [36] A. Uhlmann, *Rep. Math. Phys.* **9**, 273 (1976).
- [37] G. Gordon and G. Rigolin, *Phys. Rev. A* **73**, 042309 (2006); **73**, 062316 (2006); *Eur. Phys. J. D* **45**, 347 (2007).
- [38] F. Toscano, D. G. Bussandri, G. M. Bosyk, A. P. Majtey, and M. Portesi, *Phys. Rev. A* **108**, 042428 (2023).
- [39] D. G. Bussandri, G. M. Bosyk, and F. Toscano, *Phys. Rev. A* **109**, 032618 (2024).
- [40] C. N. Yang and C. P. Yang, *Phys. Rev.* **147**, 303 (1966).
- [41] J. Cloizeaux and M. Gaudin, *J. Math. Phys.* **7**, 1384 (1966).
- [42] A. Klümper, *Ann. Phys.* **1**, 540 (1992); *Z. Phys. B* **91**, 507 (1993).
- [43] M. Bortz and F. Göhmann, *Eur. Phys. J. B* **46**, 399 (2005).

- [44] H. E. Boos, F. Göhmann, A. Klümper, J. Suzuki, *J. Stat. Mech.* (2006) P04001.
- [45] H. E. Boos, J. Damerau, F. Göhmann, A. Klümper, J. Suzuki, and A. Weiße, *J. Stat. Mech.* (2008) P08010.
- [46] C. Trippé, F. Göhmann, and A. Klümper, *Eur. Phys. J. B* **73**, 253 (2010).
- [47] M. Takahashi, *Thermodynamics of one-dimensional solvable models* (Cambridge University Press, Cambridge, 1999).
- [48] E. Lieb, T. Schultz, and D. Mattis, *Ann. Phys.* **16**, 407 (1961).
- [49] E. Barouch, B. M. McCoy, and M. Dresden, *Phys. Rev. A* **2**, 1075 (1970).
- [50] E. Barouch and B. M. McCoy, *Phys. Rev. A* **3**, 786 (1971).
- [51] P. Pfeuty, *Ann. Phys. (New York)* **57**, 79 (1970).
- [52] M. Zhong and P. Tong, *J. Phys. A: Math. Theor.* **43**, 505302 (2010).
- [53] Z. Mzaouali, S. Campbell, M. El Baz, *Phys. Lett. A* **383**, 125932 (2019).
- [54] N. M. Millen, R. P. Rundle, J. H. Samson, T. Tilma, R. F. Bishop, M. J. Everitt, *Ann. Phys. (New York)* **458**, 169459 (2023).
- [55] X. Rong, J. Geng, F. Shi, Y. Liu, K. Xu, W. Ma, F. Kong, Z. Jiang, Y. Wu, and J. Du, *Nat. Commun.* **6**, 8748 (2015).
- [56] C. E. Bradley, J. Randall, M. H. Abobeih, R. C. Berrevoets, M. J. Degen, M. A. Bakker, M. Markham, D. J. Twitchen, and T. H. Taminiau, *Phys. Rev. X* **9**, 031045 (2019).
- [57] T. Xie, Z. Zhao, X. Kong, W. Ma, M. Wang, X. Ye, P. Yu, Z. Yang, S. Xu, P. Wang *et al.*, *Sci. Adv.* **7**, eabg9204 (2021).
- [58] A. Noiri, K. Takeda, T. Nakajima, T. Kobayashi, A. Sammak, G. Scappucci, and S. Tarucha, *Nature* **601**, 338 (2022).
- [59] X. Xue, M. Russ, N. Samkharadze, B. Undseth, A. Sammak, G. Scappucci, and L. M. Vandersypen, *Nature* **601**, 343 (2022).
- [60] M. T. Mađzik, S. Asaad, A. Youssry, B. Joecker, K. M. Rudinger, E. Nielsen, K. C. Young, T. J. Proctor, A. D. Baczewski, A. Laucht *et al.*, *Nature* **601**, 348 (2022).
- [61] T. Xie, Z. Zhao, S. Xu, X. Kong, Z. Yang, M. Wang, Y. Wang, F. Shi, and J. Du, *Phys. Rev. Lett.* **130**, 030601 (2023).
- [62] J. M. Gambetta, J. M. Chow, and M. Steffen, *npj Quantum Inf.* **3**, 2 (2017).
- [63] Y. Ohno, R. Terauchi, T. Adachi, F. Matsukura, and H. Ohno, *Phys. Rev. Lett.* **83**, 4196 (1999).
- [64] R. Hanson, B. Witkamp, L. M. K. Vandersypen, L. H. W. van Beveren, J. M. Elzerman, and L. P. Kouwenhoven, *Phys. Rev. Lett.* **91**, 196802 (2003).
- [65] A. F. Zinovieva, A. V. Dvurechenskii, N. P. Stepina, A. I. Nikiforov, and A. S. Lyubin, *Phys. Rev. B* **81**, 113303 (2010).
- [66] L. Petit, M. Russ, G. H. G. J. Eenink, W. I. L. Lawrie, J. S. Clarke, L. M. K. Vandersypen, and M. Veldhorst, *Commun. Mater.* **3**, 82 (2022).
- [67] T. Mori, T. N. Ikeda, E. Kaminishi, and M. Ueda, *J. Phys. B: At. Mol. Opt. Phys.* **51**, 112001 (2018).
- [68] J. P. Pekola and B. Karimi, *Entropy* **26**, 429 (2024).
- [69] M. Motta, C. Sun, A. T. K. Tan, M. J. O'Rourke, E. Ye, A. J. Minnich, F. G. S. L. Brandão, and G. K.-L. Chan, *Nat. Phys.* **16**, 205 (2020).
- [70] R. Sagastizabal *et al.*, *npj Quantum Inf.* **7**, 130 (2021).
- [71] C.-F. Chen, M. J. Kastoryano, F. G. S. L. Brandão, and A. Gilyén, e-print arXiv:2303.18224 [quant-ph].
- [72] X. Wang, X. Feng, T. Hartung, K. Jansen, and P. Stornati, *Phys. Rev. A* **108**, 022612 (2023).
- [73] G. A. P. Ribeiro and G. Rigolin, in preparation.